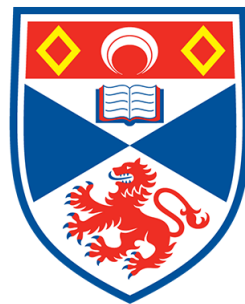# Advanced 3D Monte Carlo Algorithms for Biophotonic and Medical Applications

Lewis McMillan

University of
St Andrews

This thesis is submitted in partial fulfillment for the degree of
PhD
at the
University of St Andrews

August 2019

Declaration

I, Lewis McMillan, hereby certify that this thesis, which is approximately 34067 words in length, has been written by me, that it is the record of work carried out by me, or principally by myself in collaboration with others as acknowledged, and that it has not been submitted in any previous application for a higher degree.

I was admitted as a research student in September 2015 and as a candidate for the degree of PhD in September 2015; the higher study for which this is a record was carried out in the University of St Andrews between 2015 and 2019.

Date . . . .   Signature of candidate . . . .

I hereby certify that the candidate has fulfilled the conditions of the Resolution and Regulations appropriate for the degree of PhD in the University of St Andrews and that the candidate is qualified to submit this thesis in application for that degree.

Date . . . .   Signature of supervisor . . . .

Date . . . .   Signature of supervisor . . . .

Abstract

The Monte Carlo radiation transfer (MCRT) method can simulate the transport of light through turbid media. MCRT allows the simulation of multiple anisotropic scattering events, as well as a range of microphysics such as polarisation, and fluorescence. This thesis concerns the development of several MCRT algorithms to solve various biophotonic and medical problems. Modelling of tissue ablation, autofluorescent signals, and a theoretical quasi-wave/particle MCRT model were developed as part of this thesis.

Tissue ablation can be used to treat acne scarring and Rhinophyma, it can also be used to help enhance topical drug delivery. Currently depth of ablation is not easily elucidated from a given laser or laser power setting. Therefore, a numerical tissue ablation model is developed using MCRT, a heat diffusion model, and a numerical tissue damage model to assess ablation crater depth and thermal damage to the surrounding tissue.

Autofluorescence is the natural fluorescence of biological structures in tissue. Autofluorescence can be used as a biomarker of several diseases including: cardiovascular diseases, Alzheimers and diabetes. However, the origin of the signal is not completely clear. The effect of tissue optics on the signal, which fluorophores contribute to the signal and by how much, and how different locations on the body can effect the signal are all not well understood. This thesis presents a study of the effect of tissue optics on the autofluorescent signal. As part of this study AmoebaMCRT was created to determine the relative concentrations of fluorophores for a given autofluorescent signal.

Finally, we developed an extension to the MCRT method that allows the simulation of quasi-wave/particles. This method relies on the Huygens-Fresnel principle and the tracking of the phase of each individual photon packet. The extension, φMC, allows the modelling of complex beams that require the wave properties of light such as arbitrary order Bessel beams, and Gaussian beams. We then use φMC to predict which beam, Bessel or Gaussian, preforms "better" in a highly turbid medium.

Acknowledgements

Contents

Abbreviations

CVD cardiovascular disease.

CVDs cardiovascular diseases.

EEM excitation emission matrix.

FEM finite element method.

MCRT Monte Carlo radiation transfer.

NM Nelder-Mead.

OBS optical biopsy system.

PORH post occlusive reactive hyperemia.

List of Figures

Chapter 1

Modelling Autofluorescence in Skin for Novel Biomarkers of Cardiovascular Diseases

1.1 Introduction

Cardiovascular diseases (CVDs) are the leading cause of death in the world [1]. It is estimated that around 18 million people died in 2016 from CVDs, accounting for 31% of global deaths [1]. Despite the decreasing burden of CVDs in the UK, it was still the number two cause of death in the UK in 2014 [2].

Currently risk factors are used to try to determine if a patient has cardiovascular disease (CVD). However, these risk factors are only a "causal pathway leading to the disease" [3].

The risk factors such as high blood pressure, smoking, diabetes, physical inactivity, and dyslipidemia do not fully explain incidence of disease [4, 5]. Therefore research has moved to examining more novel biomarkers for detecting the disease. Among these novel biomarkers, the autofluorescence response of tissue is of much interest.

Autofluorescence is the natural fluorescence released by biological structures upon excitation by light. Autofluorescence is particularly attractive as a biomarker as it requires no exogenous dyes, which can be toxic, non-specific, or interfere with biological function [6]. In tissue there are several fluorophores responsible for this autofluorescent response, including: NADH (nicotinamide adenine dinucleotide), structural proteins like collagen and elastin, aromatic amino acids (tyrosine and tryptophan), porphyrins, and FAD (flavin adenine nucleotide) [7]. Changes in the autofluorescent response of tissue has been linked to cancer, Alzheimers, diabetes and CVDs [8–12]. Autofluorescence can be linked to these diseases as the fluorophores responsible for the autofluorescence either originate in the mitochondria, or are involved in important biochemical pathways that regulate apoptosis, free-radical generation, oxidative stress and biomolecular sensing of glucose, oxygen and nitric oxide.

NADH has recently been the subject of interest in particular as a biomarker for CVDs [13–15]. NADH is an intracellular co-enzyme that is a biomarker for metabolic activity, and mitochondrial anomalies. It is involved in mitochondrial function, energy metabolism, calcium homoeostasis, gene expression, oxidative stress, ageing, apoptosis and glycolysis (see Fig. 1.1). Increased amounts of NADH in tissue is indicative of oxidative stress, which in turn can indicate underlying CVDs. Therefore if there is dysfunction, then the autofluorescent signal from NADH will be

affected, thus it can be used as biomarker for disease.

Despite the appeal of using autofluorescence to diagnose and assess disease risk more research needs to be carried out on various unknowns: information on the location of fluorescence, which fluorophores contribute to the signal and how much, how much the optics of tissue affect the signal, and the variability of the signal from different locations on the body. This chapter aims to determine how much tissue optics affects the autofluorescent signal, which fluorophores contribute to the signal, and from which layer of the skin do they contribute from. Finally we introduce our ameboaMCRT algorithm, created to determine the relative concentrations of the intrinsic fluorophores in the skin to assess clinical outcomes.
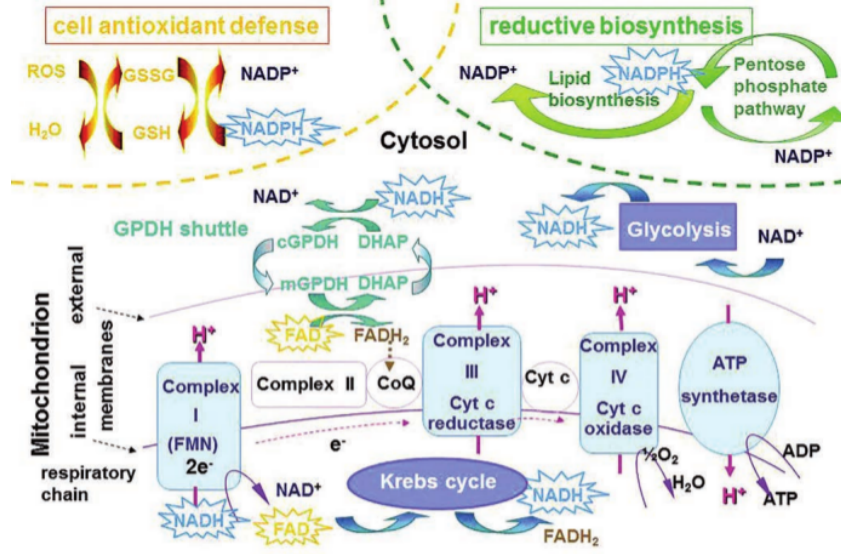
Figure 1.1: *Simplified schematic showing the roles of NADH and FAD in various different metabolic pathways. The star boxes indicate fluorescing forms of NADH and FAD. Taken from Croce et al. [16].*

1.2 Skin Model

So far in this thesis all tissue models have been simplified, by assuming that tissue is a homogeneous structure with uniform optical properties. However, this is not the case in reality. Tissue is inhomogeneous with nonuniform optical properties. However, to create a one to one model of tissue in a simulation is impractical due to the resolution required to resolve all the constituent parts of the tissue down to the cell level. Therefore, we need to make a compromise between reality and what is possible to model efficiently. This section presents a five layer model of human skin.

Dermatologists categorise the skin into several layers based upon the morphology, function, and contents of each layer [17, 18]. The layers are named from outer layer to innermost layer: stratum corneum, stratum lucidum, stratum granulosum, stratum spinosum, stratum basale, papillary dermis, reticular dermis, and hypodermis. Not all these layers are optically distinct, are too small to model or not present in a given location on the body. Therefore, we simplify this into just 5 layers: stratum corneum, epidermis, papillary dermis, reticular dermis, and hypodermis,

with the epidermis compromising of stratum lucidum, stratum granulosum, stratum spinosum, stratum basale. Figure 1.2 shows the geometry of this model.
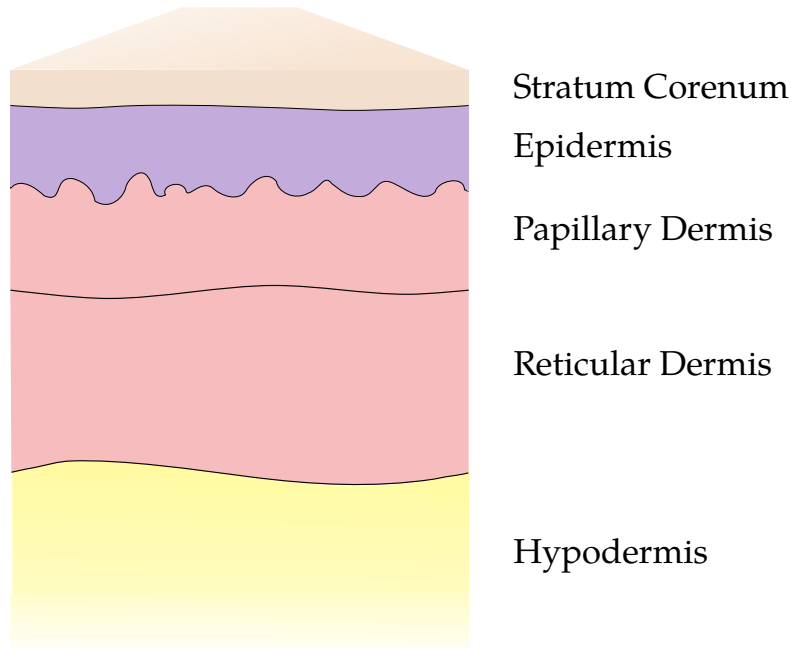
Figure 1.2: *Illustration of our five layer skin model. Image not to scale.*

Each of these layers have various amounts of chromophores and scatterers. To accurately model these various chromophores and scatterers, and therefore the skin, we must discuss the biological make-up and spatial structure of the skin.

Stratum Corenum

The outermost layer of the skin is the stratum corneum. This layer mostly consists of dead skin cells (keratinocytes). Keratinocytes, which make up approximately 80 percent of the cells in the epidermis, are born in the stratum basale and live for approximately 14 days. During this period they move upwards to the surface of the skin undergoing a series of complex morphological and metabolic events, which ends with the cells undergoing apoptosis by the time the reach the stratum corneum. The keratinocytes are flat in shape, cornified and stacked on top of each other in this layer. The function of this layer is to be a protection barrier to prevent damage, infection and diffusion of unwanted chemicals further into the skin. The stratum corneum also prevents water loss and provides some UV protection [17, 18].

Epidermis

Below the Stratum corneum is the epidermis. The epidermis consists of several layers that are optically similar so we restrict our model to modelling this as one whole layer. The layers that make up the epidermis are the stratum basale, stratum spinosum, stratum granulosum, and stratum lucidum*. Each of these layers are distinct from one another, in the fact that

---

*The stratum lucidium only appears in areas of the body where skin is thick, e.g the palm or the sole of the foot.

the keratinocytes in each layer are different from one another. In the stratum lucidium the keratinocytes are dead, and fairly flat. In the stratum granulosum the keratinocytes are grainy are becoming fairly flat in comparison to the layers below. In the Stratum spinosum the keratinocytes appears spiny (hence the name of the layer), and are polyhedral in shape. It is in the stratum spinosum that the cells begin to become keratinized and start the process of dying as they move upwards. Finally, the last layer of the epidermis, the stratum basale, is the layer where the keratinocytes are born. Here the keratinocytes are columnar or cuboid in shape.

The purpose of the epidermis is as before to provide a protective barrier to the underlying layers. In the stratum basale there are also melanocytes which produce the pigment melanin which is responsible for the color of the skin, and providing some protection from harmful UV light. Other types of cells found in the epidermis are Langerhans cells and Merkel cells which are part of the immune system and nervous system respectively. Overall the epidermis provides protection from mechanical stress, flexibility to the skin, UV protection, retains water, and stops foreign bodies or chemicals from entering the skin [17, 18].

Dermis

The dermis is the layer of skin below the epidermis, and makes up the majority of the skin by size. The cellular makeup of the dermis is different from that of the epidermis, the dermis is mostly made up of filamentous or fibrous proteins such as elastin or collagen. The dermis also contains various nerves and blood vessels. The dermis is split into three layers; the papillary dermis, the reticular dermis, and the hypodermis. The boundary between the papillary and reticular layers is demarcated by the subpapillary plexus, which is a horizontal plane of blood vessels. The boundary between the reticular and the hypodermis is marked by an abrupt change from fibrous to adipose tissue. The function of the dermis is to protect from mechanical injury, thermal regulation, contains receptors of sensory stimuli, giving the skin pliability, elasticity and tensile strength [17, 18].

1.2.1 Optical Properties

With a discussion of what makes up the skin and what molecules contribute to the skin's optical properties, this section gives an account of how our model incorporates the optical properties of skin. First we will discuss the absorbers that are found in the skin and what their absorption properties as a function of wavelength. Scattering properties of the several layers of tissue will then be discussed followed by a quick discussion on refractive indices and anisotropy values. Finally a discussion of the fluorophores found in the skin will be presented.

The first chromophore we will examine is blood. To model blood we first split blood into its deoxygenated and oxygenated components. This is done as the absorption coefficient differs between the two types of blood. We mix these two groups using the tissue oxygenation coefficient S. Blood absorption spectra are taken from S. Prahl [19]. Equations (1.1) and (1.2) give the absorption coefficients for oxygenated, deoxygenated, and whole blood.

$$\mu_{a,Oxy/DeOxy} = 150 \ \ln 10 \ \frac{\epsilon_{Oxy/DeOxy}}{64458} \qquad (1.1)$$

$$\mu_{a,blood}(\lambda) = S\mu_{a,Oxy} + (1 - S)\mu_{a,DeOxy} \qquad (1.2)$$

Where:
$\epsilon_{Oxy/DeOxy}$ is the extinction coefficient of hemoglobin $[cm^{-1}]$;
64458 is the molecular weight of hemoglobin $[g \ mol^{-1}]$;

150 is the normal concentration of hemoglobin in blood $[g\ L^{-1}]$;
and $\mu_{a,Oxy}$, $\mu_{a,DeOxy}$, and $\mu_{a,blood}$ are the absorption coefficients for oxygenated, deoxygenated and blood respectively $[cm^{-1}]$.

We also include water in our skin model. Water's absorption spectrum is taken from the work of Wieliczka *et al* and Segelstein [20, 21].

The next chromophores are bilirubin and β-carotene. These chromophores are yellow/orange pigments. Bilirubin is usually responsible for the yellow skin colour seen in people with jaundice [22]. The spectra are taken from S. Prahl's compilation of PhotochemCAD data [23, 24]. Equations (1.3) and (1.4) give the absorption coefficients of bilirubin and β-carotene:

$$\mu_{a,Bilirubin}(\lambda) = \frac{\epsilon_{bilirubin}}{585}\ ln10\ C_{bilirubin} \tag{1.3}$$

$$\mu_{a,\beta-Caro}(\lambda) = \frac{\epsilon_{\beta-Caro}}{537}\ ln10\ C_{\beta-Caro} \tag{1.4}$$

Where:

$\epsilon_{bilirubin}$ and $\epsilon_{\beta-Caro}$ are the extinction coefficients for bilirubin and β-carotene respectively $[cm^{-1}]$;
585, and 537 are the molecular weights of bilirubin and β-carotene $[g]$;
finally, $C_{bilirubin}$, and $C_{\beta-Caro}$ are the concentrations of bilirubin and β-carotene in the skin $[g\ L^{-1}]$.

Melanin is the next chromophore we model. To model melanin's absorption coefficient we use Eqs. (1.5) and (1.6), taken from [25].

$$\mu_{a,eumel}(\lambda) = 6.66 \times 10^{11} \times \lambda^{-3.33} \tag{1.5}$$

$$\mu_{a,phomel}(\lambda) = 2.9 \times 10^{15} \times \lambda^{-4.75} \tag{1.6}$$

Finally we use a base absorption coefficient to model the absorption due to the other parts of the skin that contribute to its optical properties, but individually do not have a large effect. The equation for modelling this was taken from I. Sahdi [26].

$$\mu_{a,base} = 7.84 \times 10^{8} \times \lambda^{-3.255} \tag{1.7}$$

Figure 1.3 shows the absorption spectra for the above chromophores as a function of wavelength.

To create the five layer skin model we mix different amounts of the chromophores found in each layer, as described above. Equations (1.8) to (1.11) show the respective equations for the total absorption coefficient for each layer. These equations were adapted from [25, 27, 28].

$$\mu_{a,strat} = ((0.1 - 0.3 \times 10^{-4} \cdot \lambda) + (0.125(\lambda/10.)) \times \mu_{a,b}(\lambda)) \times (1. - W) + W \cdot \mu_{H_20}(\lambda) \tag{1.8}$$

$$\mu_{a,epi} = (\nu_m \cdot (\mu_{phomel}(\lambda) + \mu_{eumel}(\lambda)) + (\mu_{a,b}(\lambda) + \ln 10 \cdot \mu_{a,\beta-caro}(\lambda) \cdot C_{caro}) \\ \times (1. - \nu_m)) \times (1. - W) + W \cdot \mu_{H_2O}(\lambda) \tag{1.9}$$

$$\mu_{a,pap/ret} = ((S \cdot \mu_{a,oxy}(\lambda) + (1. - S) \cdot \mu_{a,deoxy}(\lambda) + \ln 10 \cdot \mu_{a,\beta-caro}(\lambda) \cdot C_{caro} + \\ \ln 10 \cdot \mu_{a,bili}(\lambda) \cdot C_{bili}) \cdot B + (1. - B) \cdot \mu_{a,b}(\lambda)) \times (1. - W) + W \cdot \mu_{H_2O}(\lambda) \tag{1.10}$$
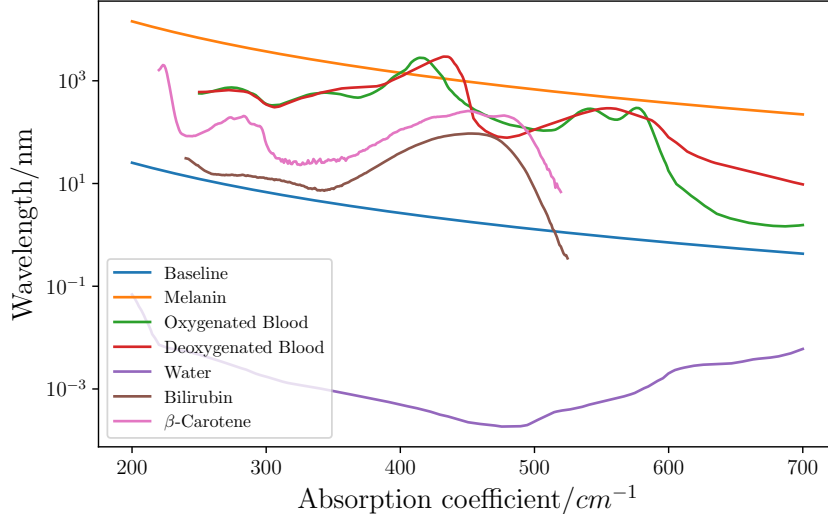
Figure 1.3: Absorption coefficients for the various chromophores found in our skin model.

$$\mu_{a,hypo} = ((S \cdot \mu_{a,oxy}(\lambda) + (1. - S) \cdot \mu_{a,deoxy}(\lambda)) \times B + \mu_{a,b}(\lambda) \cdot (1. - B)) \\ \times (1. - W) + W \cdot \mu_{a,H_2O}(\lambda) \qquad (1.11)$$

Where:

W is the volume fraction of water in a layer [-];

ν_m is the volume fraction of melanin in a layer [-];

B is the volume fraction of blood in each layer [-];

and all the other symbols have the same meanings as described above.

Table 1.1 shows the amount of each chromophore is included in each layer, and the size adopted for each layer as well as the refractive index for each individual layer. Figure 1.4 shows the total absorption coefficient as a function of wavelength for the five layers.

Layer	Thickness/ cm	Refractive index	Blood volume/%	Melanin volume/%	Bilirubin/ gL^{-1}	β-Carotene/ gL^{-1}	Water volume/%
Stratum Corenum	0.02	1.50	0.0	0.0	0.0	0.0	0.05
Epidermis	0.08	1.34	0.0	1.0	0.0	2.1e-4	20.0
Papillary Dermis	0.18	1.40	6.0	0.0	0.05	7e-5	50.0
Reticular Dermis	1.82	1.395	4.5	0.0	0.05	7e-5	70.0
Hypodermis	5.90	1.41	5.0	0.0	0.0	0.0	70.0

Table 1.1: Table of values used for the various concentrations and volumes fraction of the chromophores in the five layer skin model. Values taken from [25, 27, 29, 30].

With the absorption properties of the various chromophores in the skin defined we can now discuss the scattering properties of the skin. As the scattering properties do not vary from layer to layer by too much we use the same equation to describe the scattering coefficient [25, 28, 31].
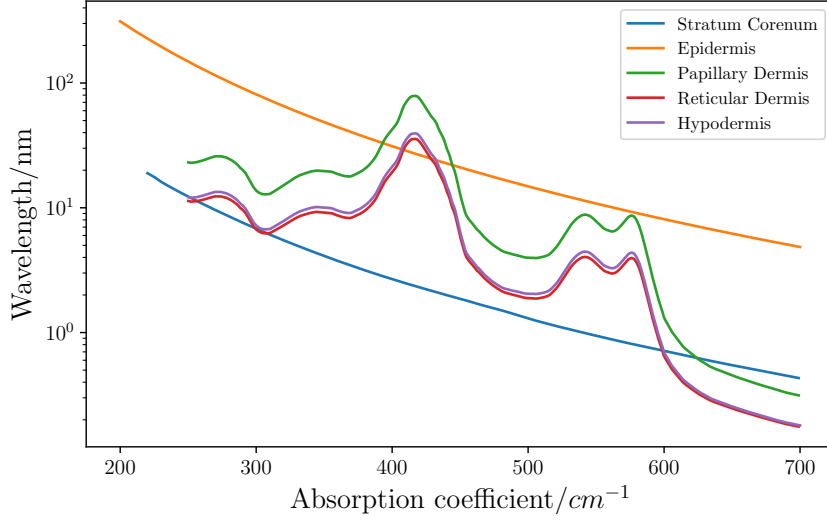
Figure 1.4: *Absorption coefficients for the different layers in our skin model.*

$$\mu'_s(\lambda) = a' \left(f_{ray} \left(\frac{\lambda}{500(nm)} \right)^4 + (1 - f_{ray}) \left(\frac{\lambda}{500(nm)} \right)^{-b_{\mathrm{mie}}} \right) \tag{1.12}$$

$$\mu'_s(\lambda) = 1050.60 \times \lambda^{-0.68} \tag{1.13}$$

Where:

μ'_s is the reduced scattering coefficient $[cm^{-1}]$;
a' is a scaling factor $[cm^-1]$;
f_{ray} is the fraction of Rayleigh scattering [-];
λ is the wavelength of light $[nm]$;
and b_{mie} is the "scattering power" [-].

This equation mixes both Mie and Rayleigh scattering into one equation. The first term represents the Rayleigh scattering terms, whilst the second represents the Mie scattering term. Figure 1.5 shows the reduced scattering coefficients for the different layers of the skin. Table 1.2 show the values used in the model for the scattering equation for the different layers.

Layer	a'/cm^{-1}	f_{ray}	b_{mie}
Epidermis	66.7	0.29	0.69
Dermis	43.6	0.41	0.35

Table 1.2: *Values of the constants for the scattering equations for the different layers of our skin model. Here epidermis represents the stratum corneum and the epidermis, and dermis represents the papillary, reticular and hypodermis in our model.*
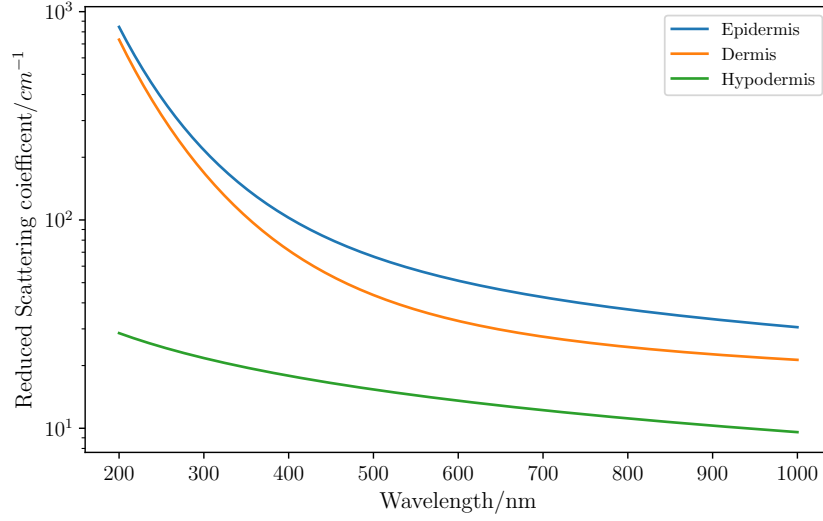
Figure 1.5: *Figure shows the reduced scattering coefficient for the different layers of our skin model.*

Finally we discuss the anisotropy values and refractive indices of our model.

First, the anisotropy g value is dependent on wavelength [31, 32] (See **??** for discussion of g values).

$$g(\lambda) = 0.62 + 0.29\lambda \times 10^{-3} \tag{1.14}$$

Where:

g is the anisotropy value $[-]$;

λ is the wavelength $[nm]$.

The refractive indices of each layer is broadly the same and does not vary form layer to layer by a large amount. Table 1.3 shows the refractive indices adopted for our skin model.

Layer	Refractive index
Stratum corneum	1.5
Epidermis	1.34
Papillary dermis	1.40
Reticular dermis	1.395
Hypodermis	1.41

Table 1.3: *Refractive indices used for the five layer skin model. Values are taken from [27].*

As information on wavelength dependent refractive indices is not readily available, we assume that the refractive indices are the same for all wavelengths used in this chapter.

1.2.2 Fluorophores in the Skin

As mentioned in the introduction there are various molecules and proteins responsible for the autofluorescent response of the skin. These include NADH (nicotinamide adenine dinucleotide), structural proteins like collagen and elastin, aromatic amino acids (tyrosine and tryptophan),

porphyrins, and FAD (flavin adenine nucleotide). Figure 1.6 shows the emission and absorption spectra for these fluorophores. As NADH and FAD are found in cells, both are typically found in all layers of the skin. Elastin and collagen are only found in the dermis [33]. Tyrosine and tryptophan are found in all layers of the skin [33].
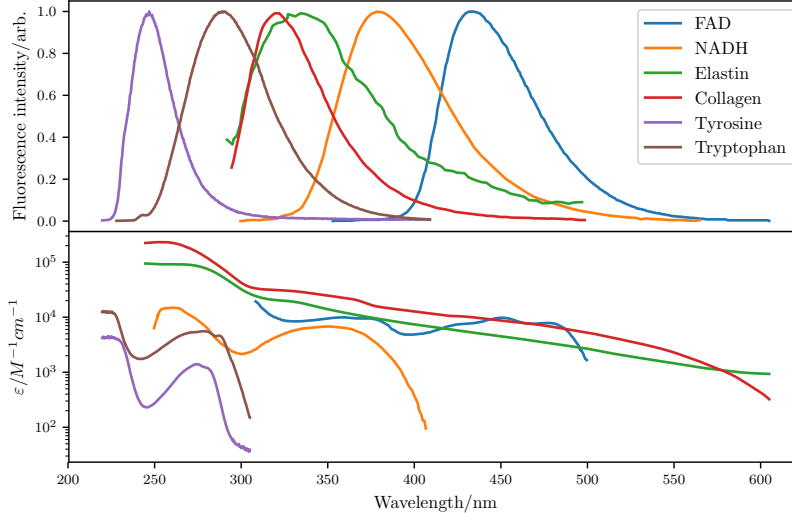
Figure 1.6: *Top) Shows the fluorescent emission for the various different fluorophores. Bottom) Extinction coefficients for a selection of fluorophores found in the skin [34–41].*

1.3   Modelling Fluorescence

Fluorescence is the process in which light of a certain wavelength is incident on a molecule, the molecule absorbs the light and re-emits the light at a longer wavelength. This process can be illustrated by a Jablonski diagram. A Jablonski diagram shows the electronic states of a molecule and the possible transitions between them. This allows the illustration of various radiative and nonradiative transitions that are possible for a give molecule, including fluorescence and phosphorescence. Figure 1.7 shows an example of Jablonski diagram for a molecule that absorbs light and re-emits it as fluorescence.

To model fluorescence from multiple fluorophores requires a change of the MCRT code presented thus far. This change is to the interaction portion of the algorithm, so that it will now include the option for a packet to undergo fluorescence. To calculate whether a packet absorbs, scatters, or fluoresces, first the probability of each of these events must be calculated. Discussion of scattering and absorption (by the bulk medium) was described in **??**. To calculate the probability of fluorescence we first assume that the quantum yield of the molecule is unity. The quantum yield of a fluorescent molecule is the ratio of photons emitted to photons absorbed. This is physically unrealistic however, it does not affect the simulations accuracy as modelling a realistic quantum yield would mean that more packets would be discarded, and thus the signal to noise ratio would be worse than if we assume a quantum yield of unity. Furthermore, information on the fluorophores used in this work, quantum yield is not readily available. To calculate the probability of fluorescence the absorption coefficient of the fluorescent molecule must be calculated. This is shown in Eq. (1.15):
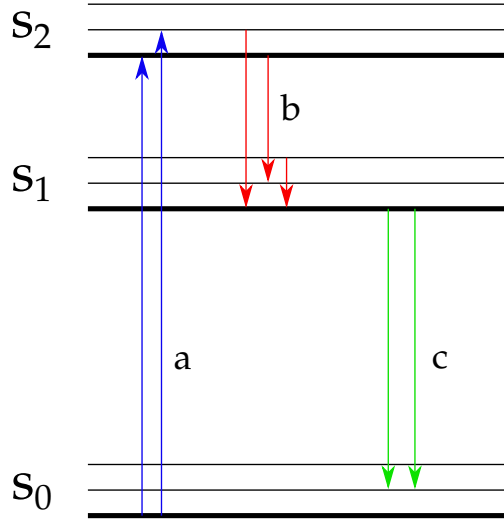
Figure 1.7: *Jablonski diagram for PPIX. Bold lines indicate the lowest vibrational state of the electronic state, and thinner lines indicate higher vibrational modes of the electronic states. a) shows excitation of the ground singlet state via absorption of a photon to the second singlet state, b) non-radiative transition, and c) fluorescence.*

$$\mu_f = \ln(10)\,\varepsilon C \tag{1.15}$$

Where C is the concentration of the fluorophore, ε is the extinction coefficient of the fluorophore, and $ln(10)$ is the natural logarithm of $10^{\dagger}$.

The next step is to calculate the total attenuation coefficient for a given species as in Eq. (1.16)

$$\mu_{t_i} = \mu_{s_i} + \mu_{a_i} + \mu_{f_i} \tag{1.16}$$

Where as usual μ_a and μ_s are the absorption and scattering coefficients, and μ_f is the fluorescence coefficient as defined in Eq. (1.15). As the absorption coefficient of fluorophores are small in comparison to the medium, and that the absorption coefficient of fluorescent molecules are generally much larger than that of their scattering coefficient, we assume that the scattering coefficient is negligible. Finally we calculate the probability of interacting with a given species using Eq. (1.17)

$$P_i = \frac{\mu_{t,i}}{\sum\limits_{i=1}^{N} \mu_{t,i}} \tag{1.17}$$

Where P_i is the probability of interacting with the ith species, the numerator is the attenuation coefficient for i^{th} species, and the denominator is the total attenuation coefficient for all the species.

Algorithm 1 shows the process used to determine which species to interact with.

[†]This factor appears as historically ε was measured in base 10 [28].

```
set μ_{t_i};
set all P_i's;
set ξ_1;
if ξ_1 <= P_1 then
    set ξ_2;
    if ξ_2 <= a_m then
        Scatter in medium;
    else
        Absorb in medium;
    end
else if ξ_1 <= P_1 + P_2 then
    Species 1 fluoresces;
else if ξ_1 <= P_1 + P_2 + P_3 then
    Species 2 fluoresces;
else if ξ_1 <= P_1 + P_2 + P_3 + ... + P_n then
    Species n fluoresces;
else
    Error, no interaction;
end
```

Algorithm 1: *An algorithm to determine which species to interact with. P_1 is the probability of interacting with the bulk medium, P_2 to P_n is the probability of interacting with a fluorescent species, a_m is the albedo of the bulk medium, ξ_i is a random number, and μ_{tot} is the total attenuation coefficient of all the species summed. The error condition should never be met.*

This method allows an arbitrary number of fluorophores to be modelled. To ensure that this method works as intended, the method is compared to experimental data taken by C.L. Campbell *et al.* [31].

C.L Campbell *et al.* filled a cuvette with Intralipid 20% diluted with water, and a fluorescent agent Coproporphyrin III. The total volume of this mixture was 6 ml, consisting of 1 ml of Coproporphyrin III, 4.99 ml of water, and 0.0 1ml of Intralipid 20%, of which 2 ml was pipetted into the cuvette. 405 nm light was shone on a cuvette of area 10 $mm \times$ 10 mm, and collected via the same fiber, of diameter 600 μm, and NA[‡] of 0.22. The signal was recorded by an optical biopsy system (OBS). The OBS uses a 405 nm laser diode ($\sim$ 1 mW output). The light was delivered by the aforementioned fiber, and fluorescent light was also collected by the same fiber.

The simulation is setup to mimic the experimental setup. The medium is uniform, so that only one voxel can be used which increases the speed of computation. A medium has a volume of 10 mm^3 . As before Intralipid is assumed to be wholly scattering with no absorption, so an albedo of 1 is used. Conversely the Coproporphyrin III is wholly absorbing with no scattering. Coproporphyrin III absorption spectrum is as shown alongside its emission spectrum in Fig. 1.8. If a photon packet leaves the top face of the simulated medium, within the radius of the fiber at an angle the fiber could accept, then the packet is recorded. The simulation is run with 10^7 photons which yielded Fig. 1.9. The algorithm presented above gave a good fit to the experimental data.

[‡]NA is the numerical aperture. The numerical aperture is a measure of the range of angles that a system can accept light.
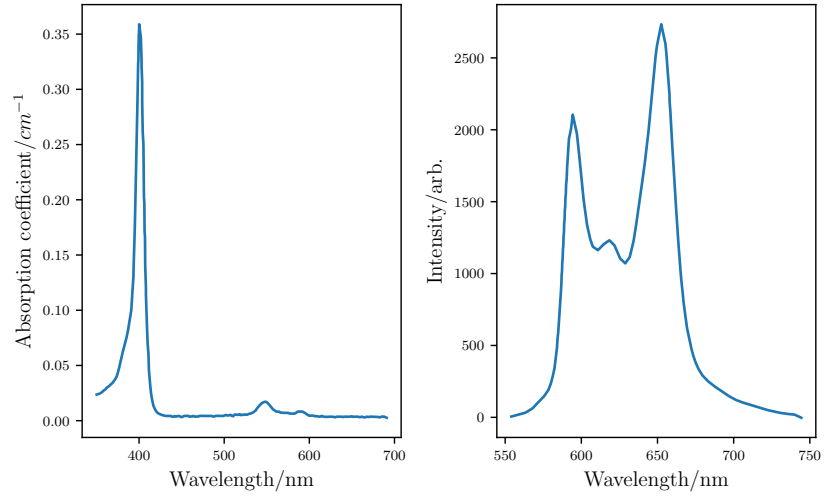
Figure 1.8: *Optical properties of Coproporphyrin III. The figure on the left shows the absorption coefficient as a function of wavelength. The figure on the right shows the emission spectrum as a function of wavelength.*
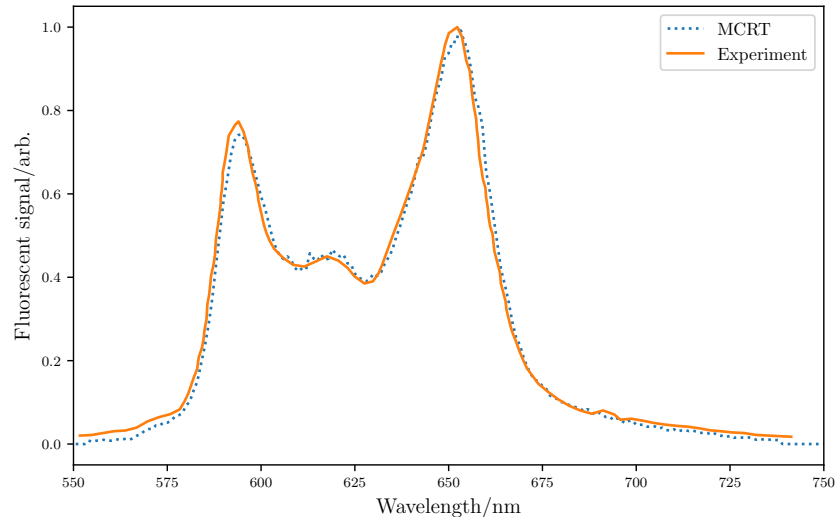
Figure 1.9: *Validation of fluorescence modelling technique as described above. Figure shows that the MCRT method matches closely to the experimental results.*

1.4   Nelder-Mead Method

To determine the contribution of individual fluorophores and their concentrations, emission profiles of these fluorophores cannot simply be fitted to autofluorescence signals. This is due to the nonlinear effect that tissue optics have on the emission profiles. Therefore, MCRT can be used to compute this effect. This leaves the problem as an optimisation problem. The Nelder-Mead method is an algorithm for unconstrained optimisation. The algorithm is based upon iteratively updating a simplex. A simplex is a structure in *n-dimensional* space, consisting of $n+1$ points. Therefore in 1D, the simplex is a line, in 2D a triangle, in 3D a tetrahedron, etc. The Nelder-Mead method is a gradient free method, meaning that it does not require derivatives to be calculated and that the search space does not need to be smooth. This makes it ideal for problems where derivatives are not able to be computed easily, or the search space is not smooth. However, the NM method can also get stuck at local minima so care must be taken to avoid this. Genetic algorithms, which do not easily get stuck in local minima, were trialled but the computational cost of using them made it unfeasible.

The NM algorithm works by removing the worst vertex of the simplex and replacing it with a "better" vertex calculated via a number of different operations. These operations can be seen in Fig. 1.10.

The first step of the NM method is to sort the initial vertices according to their fitness. For $n = 2$, we define x_w as the "worst" point, x_l and the "lousy" point, and x_b the "best" point, such that $f(x_b) \leq f(x_l) \leq f(x_w)$, where $f(x)$ is evaluating the 'fitness' of a point x. The fitness function varies from problem to problem, and usually takes the form of the function that is being optimised.

With the vertices sorted, the centroid of the simplex is calculated as in Eq. (1.18). The centroid is the mean of all the vertices except the "worst" point.
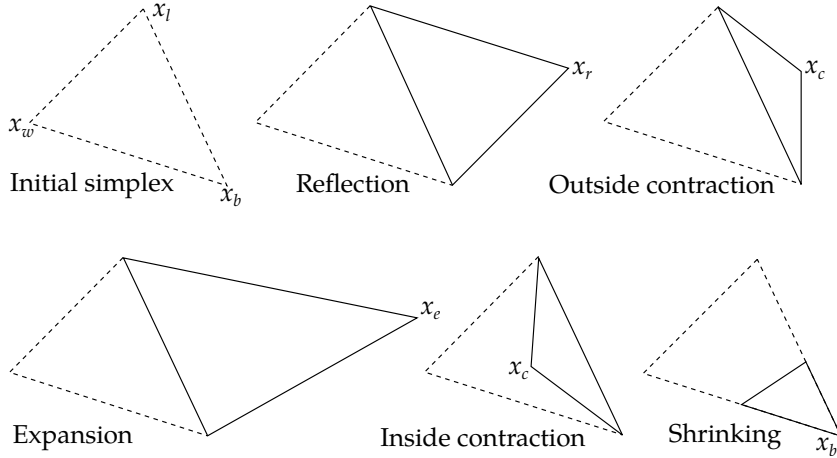
Figure 1.10: *Operations that can be performed on a simplex for $n = 2$.*

The next step is to move the simplex via a reflection. To calculate the new vertex via reflection Eq. (1.19) is used, where α is the reflection factor. If this new point, x_r, is better[§] than the current "best" point then we calculate a new point in the same direction but further using the expansion operation Eq. (1.20), where γ is the expansion factor. If this new point, x_e,

---

[§]Here better means the point has a lower fitness score.

is better than the "best" point then we replace x_w with x_e and start the process again. However, is x_e is not better than the "best" point, then we discard it and replace the worst point with x_r the reflected point.

If when calculating x_r, we find that it is worse than the "best" point, we then check if x_r is better than the 'lousy' point. If x_r is better than x_l then we replace the "worst" point and start the process again. However, if the x_r is worse than x_l, we then compare it to the "worst" point. If x_r is better than the "worst" point then we preform and inside contraction Eq. (1.22), where β is the contraction factor. If this new point, x_{ic}, is better than the "worst" point then we keep it, otherwise we preform the shrink operation, shrinking the whole simplex around the "best" point.

If x_r is not worse than the "worst" point then we preform an outside contraction Eq. (1.21). This computes a new point x_{oc}. If x_{oc} is better than x_w, then we keep it, otherwise again we shrink around the "best" point. The process described above is summarised in Fig. 1.11.

$$c = \frac{1}{n} \sum_{i=1, i \neq w}^{n+1} x_i \tag{1.18}$$

$$x_r = c + \alpha(c - x_w) \tag{1.19}$$

$$x_e = c + \gamma(x_r - c) \tag{1.20}$$

$$x_{oc} = c + \beta(x_r - c) \tag{1.21}$$

$$x_{ic} = c + \beta(x_w - c) \tag{1.22}$$

Standard values for the factors are: $\alpha = 1$, $\beta = \frac{1}{2}$, $\gamma = 2$, and $\delta = 0.5$. Though in practice these values are adjusted for the problem at hand. For higher dimensions, i.e. where $n > 2$ F. Gao *et al.* suggest that the parameters should be changed based upon how many dimensions are used for the simplex [42]. The values F. Gao *et al.* suggest are: $\alpha = 1$, $\beta = 1 + \frac{2}{n}$, $\gamma = 0.75 - \frac{1}{2n}$, and $\delta = 1 - \frac{1}{n}$. Where n is the order of dimensions. Therefore, we adopt F. Gao *et al.* values for $n > 2$ and the "standard" values for n less than equal to 2.

As the Nelder-Mead method has no inbuilt convergence criteria, this must be added. We use two different criteria based upon simplex size, and vertex fitness. The size of the simplex is calculated using Eq. (1.23):

$$size = \sum_{i=1}^{n+1} |p_i - p_{i+1}| \tag{1.23}$$

Where p_i and p_{i+1} are vertices in the simplex that are connected by an edge. If the size of the simplex falls below a pre-set value, then we preform a factorial test to see if the simplex should be restarted or if the algorithm should terminate. The factorial test checks the space around the current simplex to ensure that we have converged to a global minima. If the check fails then the algorithm is restarted with the current best point kept, and new vertices generated.

The other convergence criteria is a check to see if the best point is "good enough". The current best point is compared to a pre-set fitness value. If the best point is better than the pre-set value then the algorithm terminates.

14
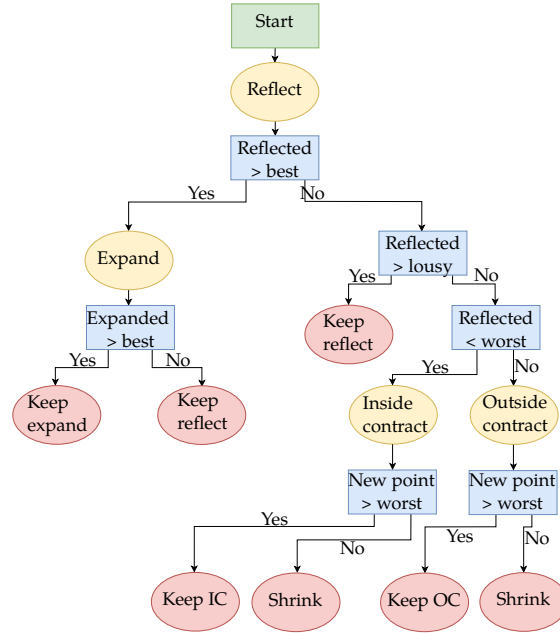
Figure 1.11: *Nelder-Mead decision tree. Here > means better, and < worse. Best, lousy, and worst have the same meanings as in the main text.*

1.5 Validation

The NM method was coded in modern Fortran, so that it could be easily interfaced with the MCRT code developed as part of this thesis. To test that the NM method works as intended a number of trial optimisation functions were tested, see Table 1.4. This was achieved by selecting an initial simplex, and the method allowed to iterate until it converged. The results of this are shown in Fig. 1.12.

Name	Formula	Global Minimum
Sphere	$x^2 + y^2$	$f(0,0) = 0.$
Rosenbrock	$(a - x)^2 + b(y - x^2)^2$	$f(1,1) = 0.$
Ackley	$-20 \exp \left[-0.2 \sqrt{0.5 \left(x^2 + y^2 \right)} \right] -$ $\exp \left[0.5 \left(\cos 2\pi x + \cos 2\pi y \right) \right] + e + 20$	$f(0,0) = 0.$
Himmelblau's	$(x^2 + y - 11)^2 + (x + y^2 - 7)^2$	$f(3,2) = 0.,$ $f(-2.805118, 3.131312) = 0.,$ $f(-3.779310, -3.283186) = 0.,$ $f(3.584428, -1.848126) = 0.$

Table 1.4: *Table of standard test functions for numerical optimisation.*

Some of these functions (Sphere, and Rosenbrock's) can also be extended to arbitrary dimensions. These functions were used to check that the NM method works as intended in these higher dimensions where the NM method will primarily be used in this thesis.

To ensure that the NM method can be used to find the unknown concentrations of the autofluorophores, we test the method with two different toy models. The first model is a "2D"
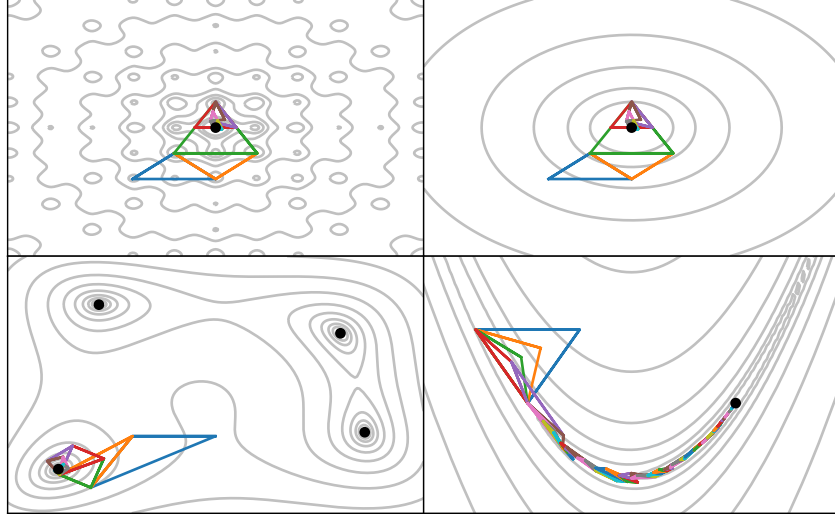
Figure 1.12: *Contour plots of test functions with Nelder-Mead simplicies over plotted. Top left is the Ackley function, top right is the sphere function, bottom left is the Himmelblau's function, and the bottom right is the Rosenbrock function. Grey lines are contours, coloured lines are the simplicies with the blue simplex being the initial simplex. Finally, the black dots represent the global minima for that function.*

model, with two different fluorophores evenly distributed over all 5 layers of our skin model, i.e $n = 2$. The two different fluorophores are NADH, and a fictitious fluorophore that has similar properties to FAD and tryptophan, such that the excitation spectrum is that of FAD and the emission spectrum is that of tryptophan. The concentration in these layers is such that the bulk optical properties are not affected: NADH has a concentration of 1.0 μM, and the fictitious fluorophore has a concentration of 2.5 μM. To generate a spectrum to which the NM method can compare to, the MCRT code is run with the above configuration of fluorophores. This generated Fig. 1.13.
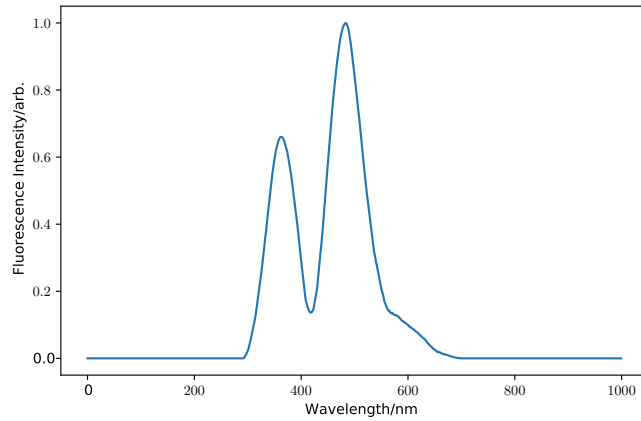
Figure 1.13: *Example of toy model spectrum for testing NM method. The two peaks correspond to the fictitious fluorophore, and NADH.*

The fitness function chosen to check whether the NM method is converging to the generated spectrum is as:

$$fitness = \sum_{i=1}^{n}(x_i - m_i)^2 \qquad (1.24)$$

Where x_i is a data point at a wavelength λ_i produced by the MCRT, and m_i is a data point in the model at a wavelength λ_i.

As the NM can get stuck in local minima, we run the method for several different initial simplices to ensure that this does not occur. As the MCRT code is called multiple times per simplex iteration, and the fluorophore concentration is low meaning that many packets need to be run to achieve a good signal to noise ratio. These two conditions result in a computational load that is infeasible to run. Therefore the MCRT algorithm has to be computationally efficient in order to arrive at an answer within a reasonable time. As the optical properties only vary in the z direction, the voxel model is shrunk to $1 \times 1 \times 500$, with 500 voxels representing the z direction. To this end the 3D skin model is shrunk to a 1D model in the z direction so that the optical integration routine can efficiently move the packet through the simulated medium. The optical properties of the incident wavelength are also stored so that when a new packet is started the optical properties can easily be adjusted without need for any calculation. Finally a filter is employed on the output fluorescence spectrum to smooth the noise out.

The filter used is a Savitzky-Golay filter. This filter fits multiple low-degree polynomials to subsets of the data, thus smoothing the data [43]. Equation (1.25) shows the functional form of the Savitzky-Golay filter, where for a data set consisting of n (x_j, y_j) points, and C_i are the set of m convolution coefficients. m is the "window" of data the polynomial of order k if fitted to via the linear least squares method.

$$Y_j = \sum_{i=\frac{1-m}{2}}^{\frac{m-1}{2}} C_i y_{j+1} \qquad (1.25)$$

Figure 1.14 shows the use of the Savitzky-Golay filter on sample output data from the MCRT simulation.

Using the above set-up with the Savitzky-Golay filter on the output spectrum, allowed the NM method to efficiently run many models of various different concentrations and "find" a set of concentrations that resulted in a close match with the target spectrum. However, as the detected fluorescence spectra are normalised to their peak values we cannot use this method to determine the original concentration, but rather the ratio between the two concentrations. Figure 1.15 shows the search space and the spread of the concentration values calculated by the NM method compared to the original target concentrations. The spread of the concentrations calculated by the NM method follow a linear relationship as would be expected. Therefore, a line of best fit was fitted to the concentrations. This yielded a line ($y = m\ x$) with $m = 2.49 \pm 0.05$. The expected relation between the concentration is where $m = 2.5$ therefore, the NM method can be used to determine the relative difference in concentrations within one standard deviation.

The NM method was also tested on a toy model for $n = 3$. Here the fluorophores used were: NADH, FAD, and a fictitious fluorophore with the absorption properties of NADH and the emission properties of Tyrosine. The fluorophores had concentrations of $1.05\mu M$ $525\mu M$, and $125\mu M$ respectively. The set-up is the same for the above $n = 2$ case, with the same filter and computational speed ups used. Figure 1.16 shows various concentrations as calculated by the NM method compared to the original concentration. Again a line of best fit was fitted to
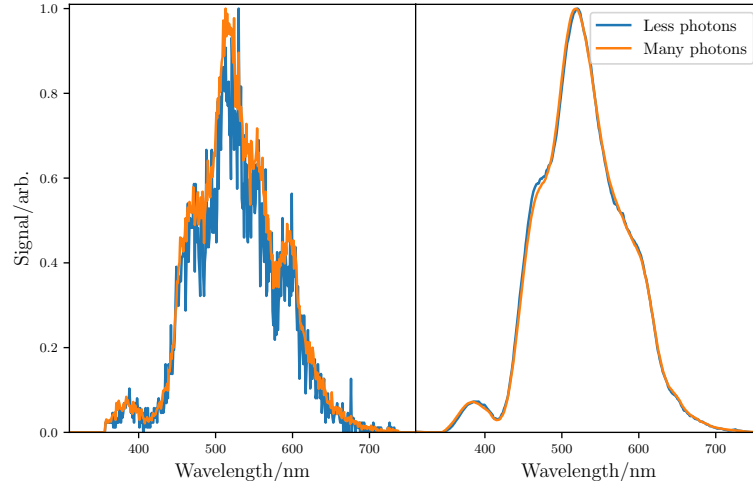
Figure 1.14: *Illustration of how the Savitzky-Golay filter works on noisy data and recovers the roughly the same signal on the same data set with less noise. Left image shows the raw signals from the simulations with a packets difference of 10^{-3}. Right image shows the data set after the Savitzky-Golay filter is applied. A window size of 101, and polynomial of order 2 were used as the filter settings.*
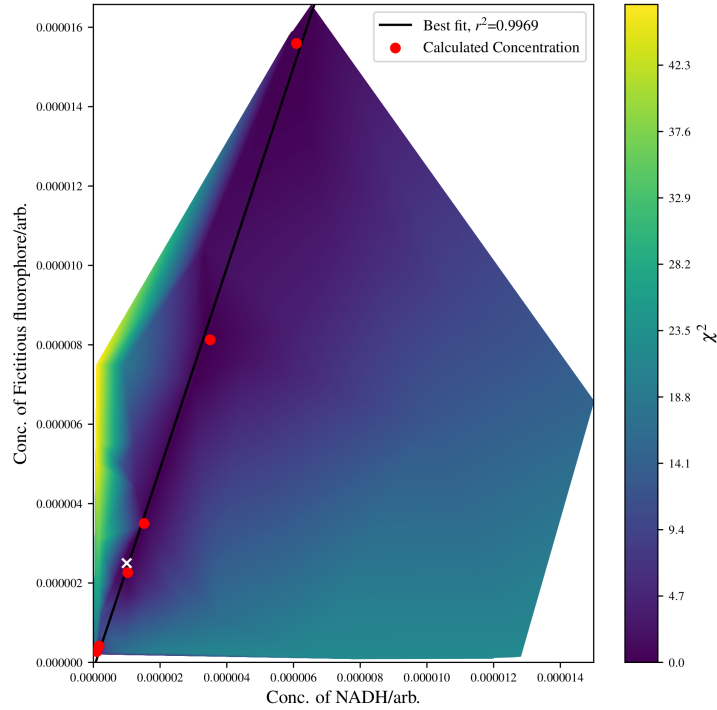
Figure 1.15: *Figure shows the search space for the 2D toy problem outlined above. A line of best fit is fitted to the concentrations found by the NM method. Note also the valley of good fit where the line of best fit lies. The search space is also fairly smooth.*

18

the calculated points ¶. As there is no closed form solution for the equation of a line in $n > 2$ dimensions, the equation of a line in 3D can be represented by Eq. (1.26):

$$\overrightarrow{r} = \overrightarrow{r_0} + t \overrightarrow{v}$$

(1.26)

Where $\overrightarrow{r}$ and $\overrightarrow{r_0}$ are position vectors for P and P_0 respectively, $\overrightarrow{v}$ is a vector parallel to the line we are examining, and t is some real number. This equation also holds for an arbitrary number of dimensions. The line of best fit yielded $\overrightarrow{v} = [0.0013, 0.9858, 0.1682]$. Where as the "real" $\overrightarrow{v}$ is equal to $[0.0019, 0.9728, 0.2316]$. This again shows that the NM method can be used to find the relative concentrations of the fluorophores in the skin, even in dimensions higher than 2.
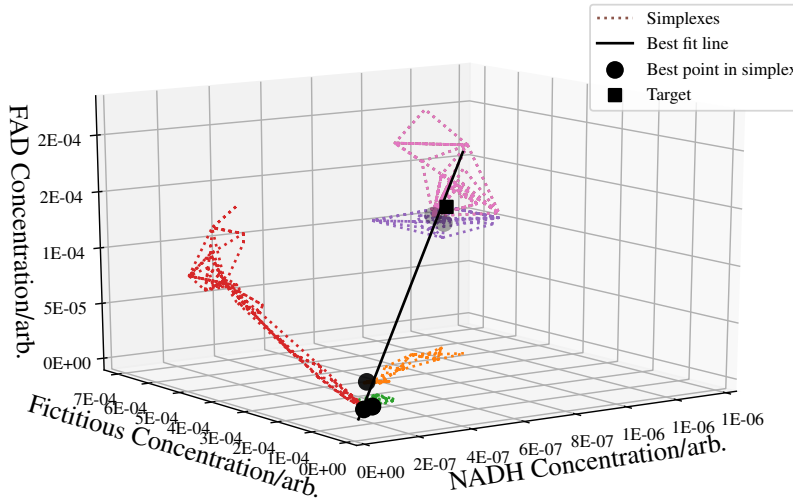
Figure 1.16: *Figure shows the line of best fit for the case where $n = 3$. Figure also shows the simplices path over their whole lifetime, from initial guess to final simplex.*

1.6 Results

1.6.1 Experimental Work

Experimental work discussed in this section was carried out by my collaborators S. Smirni *et al.* at the University of Dundee and Ninewells Hospital.

S. Smirni *et al.* took autofluorescence spectra from the volar forearms of volunteers using the LAKK-M multi-functional laser non-invasive diagnostic system (MLNDS). The LAKK-M system combines laser-Doppler flowmetry, tissue reflectance oximetry, pulse oximetry, and laser fluorescent diagnostics in one machine. The LAKK-M system delivers and collects light via the same optical fiber package. The fiber package has seven optical fibers, one for each probing wavelength (365 nm, 430 nm, 532 nm, 635 nm), two detectors, and a spectrometer. The fibers radii are 0.4 mm, and the separation between the fibers is around 1 mm. S. Smirni *et al.* took autofluorescence spectra from volunteers as they underwent a post occlusive reactive hyperemia (PORH) test. A PORH test is used to investigate and assess microvascular function. It achieves this by usually inflating a cuff on an arm of a patient for a period of time and then letting it

---

¶The line of best fit was calculated using the singular value decomposition (SVD) method of solving the least squares.

deflate. Whilst this is happening laser Doppler flowmetry is used to assess the flow of blood before inflation, during inflation and after inflation. How the micro-vascular system responds to this test can be indicative of various CVDs. Figure 1.17 shows an example of the data collected during a PORH test.
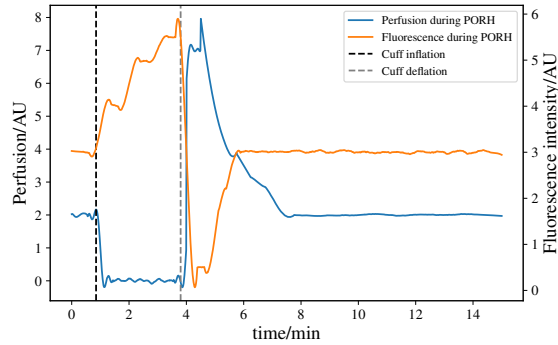
Figure 1.17: *Example of a PORH test whilst measuring autofluorescence and perfusion. The perfusion of blood in the skin decreases once the cuff is inflated, and then rapidly reaches a maximum once the cuff is removed. The inverse of this can be seen in the autofluorescent response of NADH in the tissue.*

S. Smirni collected around 27 spectra at the rate of 1 per minute over a period of 27 minutes as the PORH test was undertaken, 11 for a baseline before inflation of the cuff, 5 during occlusion and 11 post occlusion. Spectra were taken at each of the possible wavelengths (635 nm, 532 nm, and 365 nm) that the LAKK-M provides, yielding a total of 81 autofluorescence spectra per volunteer. S. Smirni also collected laser Doppler flowmetry data during this period, however as this work only concerns the modelling of autofluorescence, we restrict the analysis to that of the UV (365 nm) autofluorescence spectra. Figure 1.18 shows an example of a raw spectrum taken during the baseline portion of the experiment.
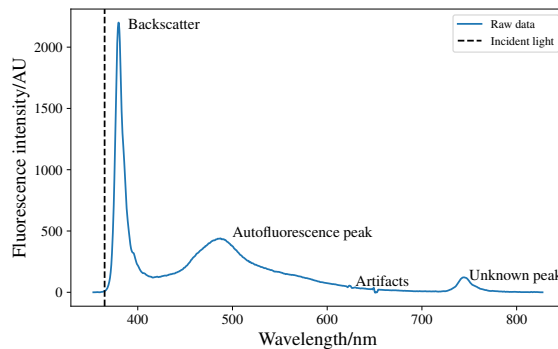
Figure 1.18: *Figure shows an example of a raw spectrum taken by S. Smirni et al.. This figure illustrates how the spectrum is red-shifted, along with some of the artifacts, backscatter, and autofluorescence peaks. There is also a third peak in the red end of the spectrum. The cause of this is unknown, but most likely due to an unidentified fluorophore.*

1.6.2 Effect of Tissue Optics on Fluorescent Signal

As mentioned in the introduction to this chapter information about how tissue optics affects the fluorescent signal, which fluorophores contribute to the signal, the variability of the signal in different test sites, and location of the fluorescent signal are not well elucidated. Therefore, before running the NM method on the experimental data, we analyse these various unknowns. We also present results on how the excitation wavelength affects the signal.

Figure 1.19 shows the fluence as a function of depth for the incident UV light. The figure shows that most of the incident light is contained within the top three layers, with little getting to the Reticular dermis, with none reaching the Hypodermis. The fluence drops to 50% of its peak value 0.026 cm into the tissue which equates to inside epidermis, and 10% of its peak value by 0.058 cm into the tissue which again is in the epidermis.
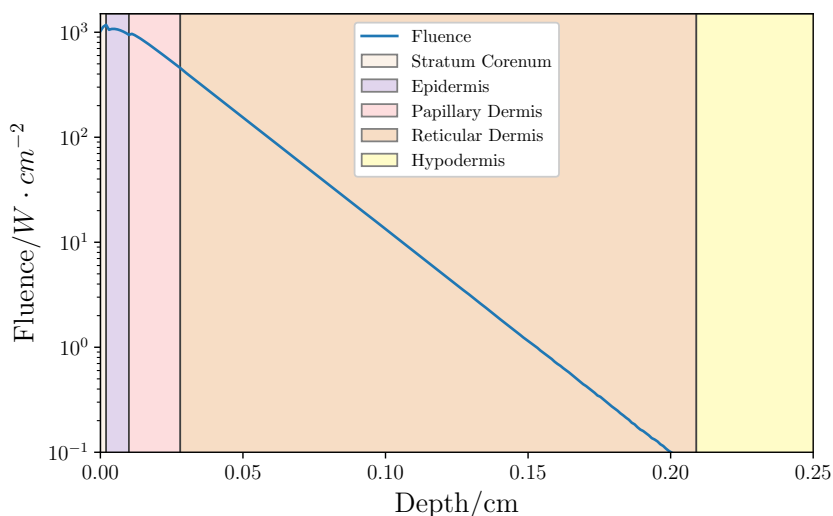
Figure 1.19: *Penetration of UV radiation as a function of depth.*

Figure 1.20 shows the fluence$^{\parallel}$ of detected fluorescent light (see ?? for discussion of how this is tracked). The figure shows the fluence of light for each fluorophore that is detected. The figure shows that the fluence is highest in the Papillary dermis and a number of peaks at the boundaries of the layers. First the refractive indices of the layers are different, this can lead to light getting "trapped" in a layer as it can be internally reflected off the layer boundary, thus leading to increased fluence. Second, fluorescent light is emitted isotropically which means that fluorescent light emitted in the upper layers of the skin, may be emitted in the direction of the Papillary dermis, and light emitted from below the papillary dermis has to travel though the papillary dermis in order to be detected. Finally the optical properties also have an effect on the detected light fluence. The dermal layers have a minimum in their absorption spectra at the range of wavelengths that NADH and FAD emit at, thus light is more likely to "survive" through the dermal layers than the other layers such as the epidermis. Finally the geometry of the layers most likely has an effect as well. The stratum corneum's and the epidermis's thickness is small in comparison to that of the dermal layers, thus there will be less fluorescent light emitted from these layers when the concentration are the same.

Figure 1.21 shows the location of where the fluorescent light is emitted from. For both NADH, and FAD their peaks depth is just inside the epidermis. However, the vast majority of emitted

---

$^{\parallel}$Though this is not real fluence, as all photons would contribute to the overall fluence. An accurate name for this quantity would be the contribution to the fluence by the detected fluorescence of a fluorophore.
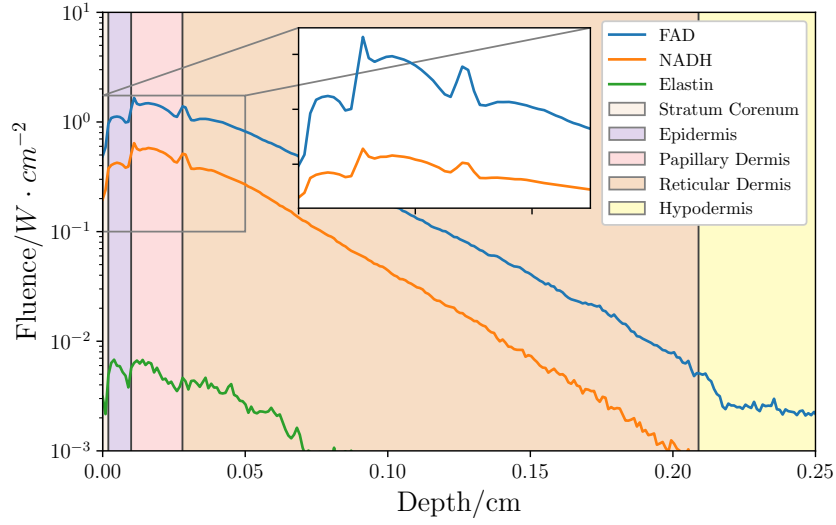
Figure 1.20: *Detected "fluence" for FAD, NADH, and elastin fluorescence. Inset shows zoom in of top layers of the skin, note the inset is a linear scale.*

Fluorescent light originates in the papillary dermis. This occurs as enough light gets to this layer, which allows more light to undergo fluorescence.
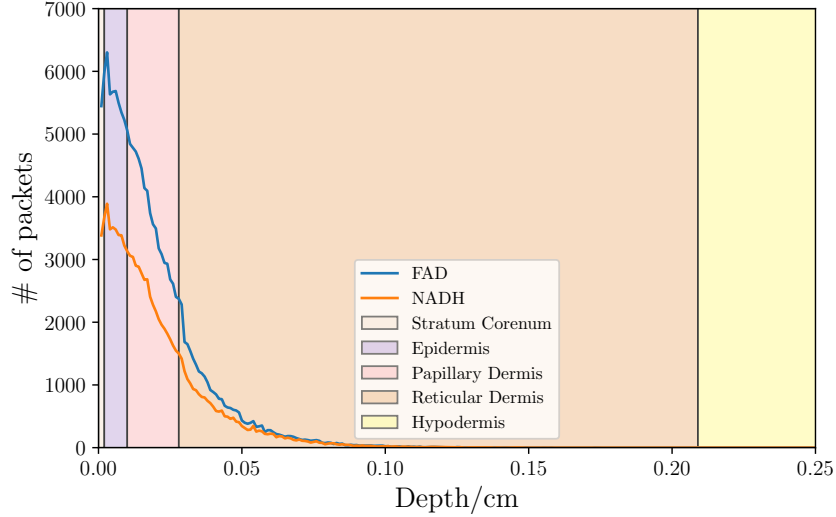
Figure 1.21: *Amount of packets escaping as a function of depth for FAD and NADH fluorescence.*

Finally, we analyse the effect excitation wavelength has on the detected signal of NADH and FAD. To achieve this we run several models in order to create an excitation emission matrix (EEM). A EEM is a way of investigating and displaying the effect excitation wavelength has on the fluorescent output of a sample. Using the same setup as above, we vary the fluorophore concentration in each layer, such that only one layer at a time has any fluorophores in it. We then excite the model over a range of wavelengths. For NADH we use wavelengths in the range of 250 to 400 nm, and for FAD we use 250 to 500 nm. Figure 1.23 show the EEM for NADH and FAD. The EEM for NADH shows that the strongest signal comes from the papillary dermis when compared to other layers. The EEM also shows a maximum of emission for excitation

wavelengths corresponding to around 260 nm and 320–380 nm. For FAD the layer that yields the most fluorescence is the reticular dermis. The EEM shows that for excitation wavelengths of around the range 450–500 nm gives the most fluorescence.

For the case of NADH the optimal excitation wavelengths coincide with maxima in the absorption spectrum of NADH (see Fig. 1.22). However, for FAD the maximum in fluorescence does not coincide with the largest maxima in its absorption spectrum (see Fig. 1.22), but rather it falls within a smaller maximum. This is because light at the maximal absorption peak (~300 nm) is highly absorbed by tissue, especially in layers such as the epidermis. Therefore, light at a longer wavelength is more likely to escape the tissue due to the tissue optical properties.
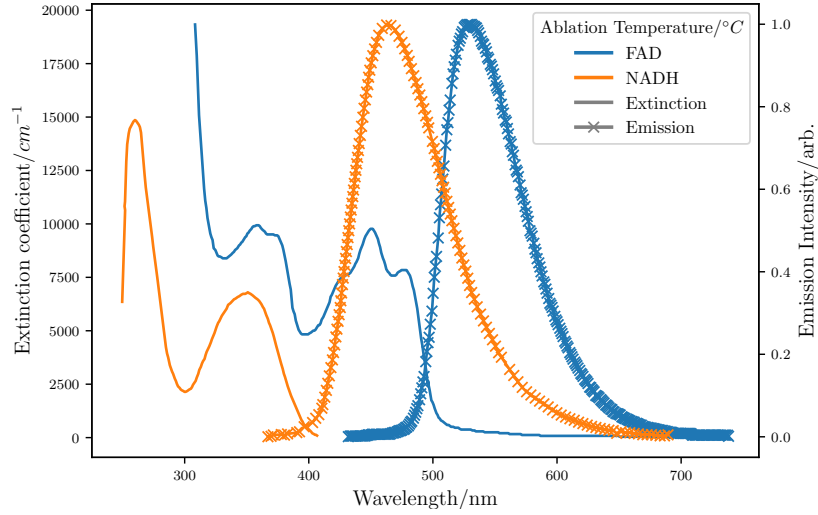
Figure 1.22: *NADH and FAD absorption and emission spectra.*
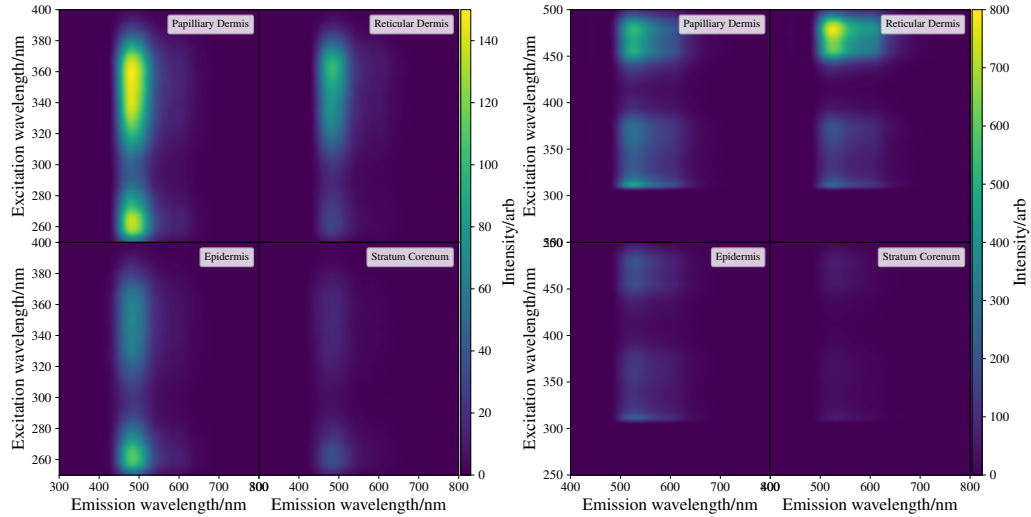
Figure 1.23: *Left) Excitation-emission matrix for NADH. Figure shows that the fluorescent signal from NADH is strongest in the papillary dermis. Right) Excitation-emission matrix for FAD. Figure shows that the fluorescent signal from FAD is strongest in the reticular dermis.*
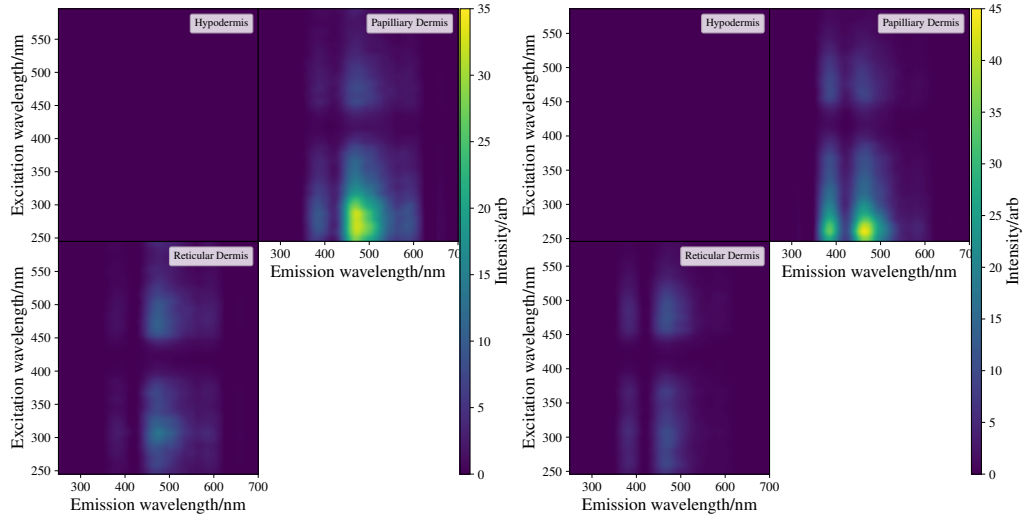
Figure 1.24: *Left) Excitation-emission matrix for Elastin. Figure shows that the fluorescent signal from Elastin is strongest in the papillary dermis. Right) Excitation-emission matrix for collagen. Figure shows that the fluorescent signal from collagen is strongest in the papillary dermis.*

Effect of Chromophores and Skin Thickness on Autofluorescent Signal

This section shows the effects of several variables of the skin on the autofluorescent signal of NADH, FAD, collagen, and elastin. The skin variables chosen are the blood volume of the skin, melanin content of the epidermis, and the thickness of skin. The effect of these variables were studied at several wavelengths, chosen as they were either the wavelength used in the experimental work (365 nm) or are peaks in the fluorophores spectrum as shown in Figs. 1.23 and 1.24. The wavelengths for each of the fluorophores are:

FAD: 310, 365, 450, 480 nm
NADH: 260, 320, 365, 380 nm
Collagen/Elastin: 260, 320, 365, 480 nm

Each of the fluorophores are uniformly distributed in the 5 layer skin model in accordance with where they are naturally occurring with a concentration of $1\mu M$. The collection geometry is the same as the experimental setup, and the Savitzky-Golay filter is used as before. 10 million photon packets were run for most of this study. However, for the melanin simulations 6.4×10^7 packets were run to achieve a good signal to noise ratio. Each spectrum calculated is then analysed to compare signal strength and signal peak as functions of the skin variables.

Blood

The first property we investigate is the effect of blood volume on the autofluorescent signal. We vary the blood volume from "normal" levels as used in our previous models, by factors of 0.0×, 0.5×, 1.0×, and 2.0×. Figures 1.25 and 1.26 show the results from these models.

As expected, as the amount of blood in the model increases the signal strength goes down for all the fluorophores. For FAD's fluorescent peak position, the amount of blood has little effect, with an overall shift of 0–6 nm. The blood volume has a larger effect on NADH's, elastin's,

Figure 1.25: *Effect of blood content on NADH (left) and FAD (right) autofluorescence. Top left of each image shows the effect of blood on signal strength. Top right of each image shows the effect of blood on location of the fluorophores peak. Bottom of each image shows the raw spectra for 365 nm.*

and collagen's peak position. NADH's peak position is shifted further into the red end of the spectrum with increasing volume of blood in the skin, with the maximum overall shift equating to $\sim 25 \; nm$. This shift occurs as there is a maximum in the blood absorption spectrum at around $410 \; nm$, and a minimum in the spectrum at 460–$500 \; nm$. Both these features of the blood absorption spectrum gives rise to the shift of the fluorescent peak in NADH shifting it to the red end of the spectrum.

Figure 1.26: *Effect of blood content on elastin (left) and collagen (right) autofluorescence. Top left of each image shows the effect of blood on signal strength. Top right of each image shows the effect of blood on location of the fluorophores peak. Bottom of each image shows the raw spectra for 365 nm.*

For elastin and collagen the autofluorescent spectra are not as simple as that of NADH or FAD. Both elastin and collagen's spectra are multi-modal. This is due to blood's effect on the signal. As shown in Fig. 1.26 the signal for no blood in the model, both consist of a single peak. When blood is introduced the signal becomes multi-modal. This is because the absorption spectrum has a maximum at $\sim 410\ nm$, and a minimum at $\sim 460\ nm$. The maximum at $410\ nm$ causes a dip in the spectrum in both elastin and collagen spectra. Conversely the maxima at $460\ nm$ for elastin and collagen is caused by the minimum in the blood absorption spectra.

Melanin

The next property we investigate is the effect of melanin on the autofluorescent signal. We use the following melanin volume fractions 1, 3, 5, 10, 20, and 30% which correspond to Fitzpatrick skin types I, II, III, IV, V, and VI respectively [25, 44]. Figures 1.27 and 1.28 show the results of this investigation.
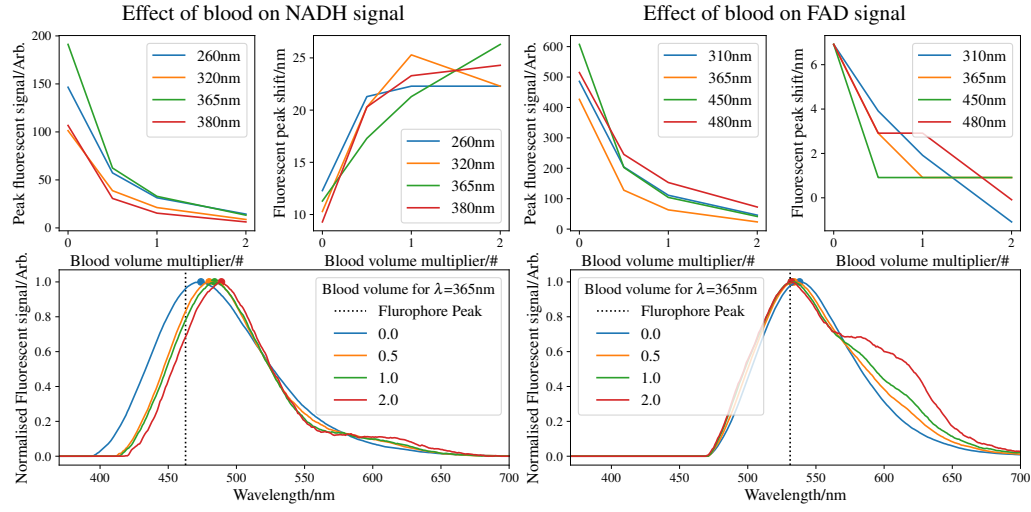

Figure 1.27: *Effect of melanin content on NADH (left) and FAD (right) autofluorescence. Top left of each image shows the effect of melanin on signal strength. Top right of each image shows the effect of melanin on location of the fluorophores peak. Bottom of each image shows the raw spectra for 365 nm.*

As the amount of melanin increases in the skin, the amount of fluorescence being collected drops exponentially, this is true for all four fluorophores. The "best" wavelengths for each of the fluorophores, i.e the wavelength that gives the strongest signal, are: NADH: $365\ nm$, FAD: $480\ nm$, Elastin: $260\ nm$, Collagen: $260\ nm$.

For both NADH and FAD increased amounts of melanin in the skin moves the peak of fluorescence into the red end of the spectrum. This is more pronounced in the NADH spectra with an overall shift of 20–45 nm compared to the -5 to 10 nm shifts for FAD. This shift can be explained by the shape of the melanin absorption curve (see Fig. 1.3). The melanin absorption curve shows that melanin absorbs more in the UV end of the spectrum, compared to the red end of the spectrum. Thus, the fluorescent signals are moved towards the red end of the spectrum where there is less absorption and therefore more chance of being detected.

For elastin and collagen the shift is not as linear. First, the shapes of the fluorescence signal for collagen and elastin are multi-modal when compared to that of FAD or NADH. The reason for the dip in the collagen and elastin spectrum at around the 400–410 nm section, is due to an absorption peak in the dermal layers due to blood as described in the previous section. Clear
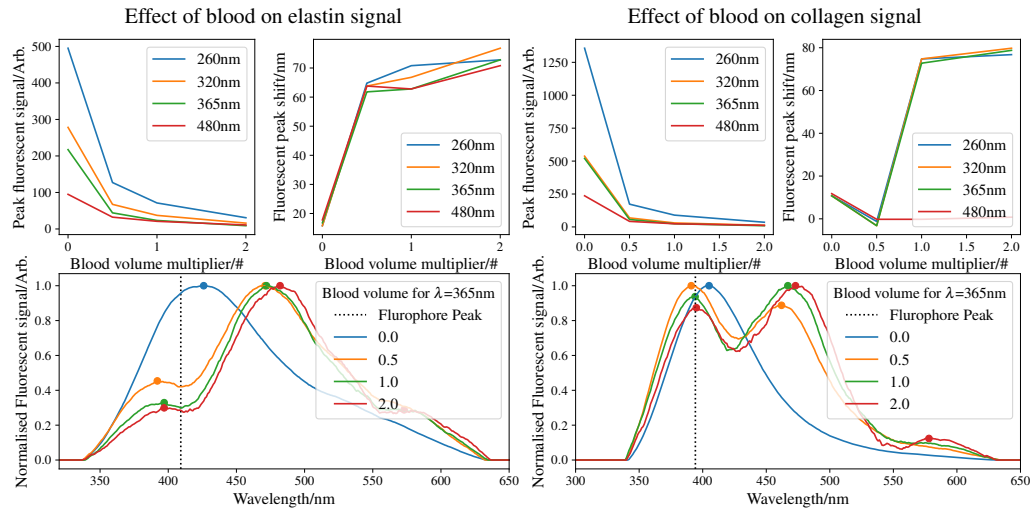
Figure 1.28: *Effect of melanin content on elastin (left) and collagen (right) autofluorescence. Top left of each image shows the effect of melanin on signal strength. Top right of each image shows the effect of melanin on location of the fluorophores peak. Bottom of each image shows the raw spectra for 365 nm.*

evidence for this can be seen in the collagen autofluorescence signal. As the amount of melanin increases, this blocks light from reaching the dermal layers therefore, the fluorescence spectrum of collagen is less affected by tissue optics due to the lower penetration. Conversely, the second peak in the collagen spectrum is due to a minimum in the absorption spectrum of blood. This again gives rise to a maximum in the collagen autofluorescence signal, which is missing in the simulations with greater amounts of melanin present for the same reasons as described above. Therefore, the peaks position is either near the original fluorescent peak or moved $\sim 60\ nm$ into the red end of the spectrum.

FAD's spectrum has two or three peaks depending on the melanin content. For the case where there is less melanin, i.e Fitzpatrick skin type I or II, there are three well defined peaks. Whereas for skin types V and VI, there are two less well defined peaks. This is due less photon packets detected, giving rise to a flatter profile for the signal at higher amounts of melanin. As mentioned above, the dip at $410\ nm$ is due to the absorption peak in blood. The main peak in the FAD signal is at around $460\ nm$, which coincides with a minimum in the absorption spectrum of blood. Finally the peak at around $580\ nm$ is again due to a minimum in the blood absorption spectrum. As the melanin content increases this leads to light not penetrating into the dermis, therefore the signal lacks these features at higher volumes of melanin.

Skin Thickness

The final property we investigate is skin thickness. The thickness of skin varies over different locations on the body. It also varies with age, ethnicity and sex [45–47]. Therefore, to get an idea of how the skins thickness effects the autofluorescent signal we trial three different thicknesses. For thin skin we use measurements taken from the eyelid's of people of Korean ethnicity [45]. For thick skin we use measurements taken from the back's of people of Anatolian ethnicity [46]. Finally, the skin thickness we have used in all previous models is approximately that of the back skin of people of Korean ethnicity [45].

Figures 1.29 and 1.30 show some of the results of the effect of skin thickness on the aut-
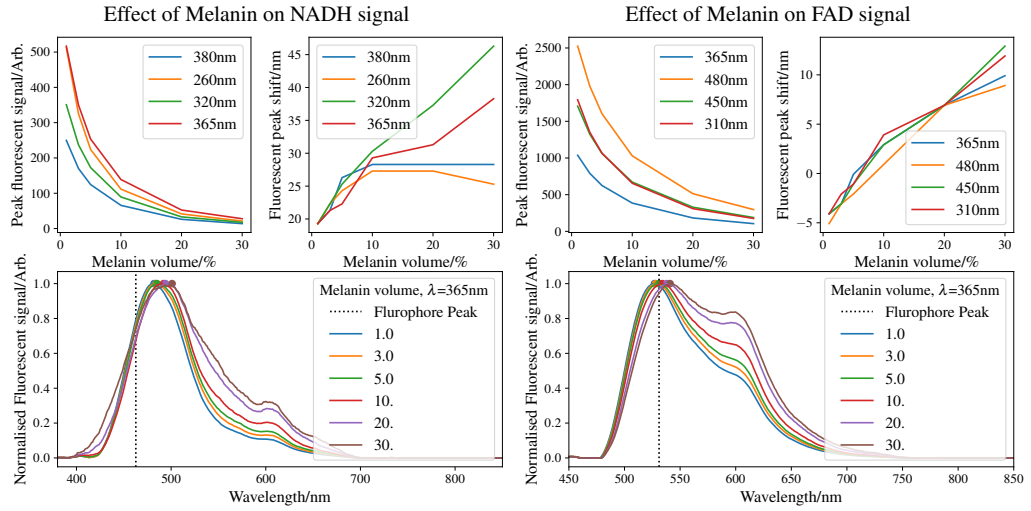
Figure 1.29: *Effect of thickness on NADH (left) and FAD (right) autofluorescence. Top left of each image shows the effect of skin thickness on signal strength. Top right of each image shows the effect of skin thickness on location of the fluorophores peak. Bottom of each image shows the raw spectra for 365 nm.*

ofluorescent signal from several fluorophores used in this study. NADH and FAD peaks are not affected by differing thickness of skin (NADH peak is shifted overall $\sim 20\ nm$), with the variation between thick and thin skin only being around 3 nm. As may be expected the main difference between thick and thin skin is the strength of the signal. Thinner skin gives rise to a stronger autofluorescent signal, whereas thicker skin gives a weaker signal as would be expected.

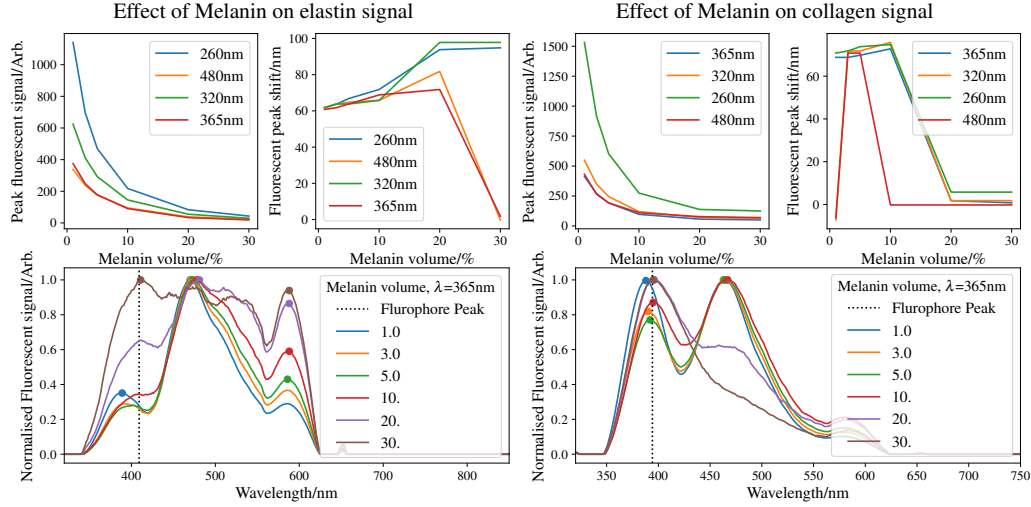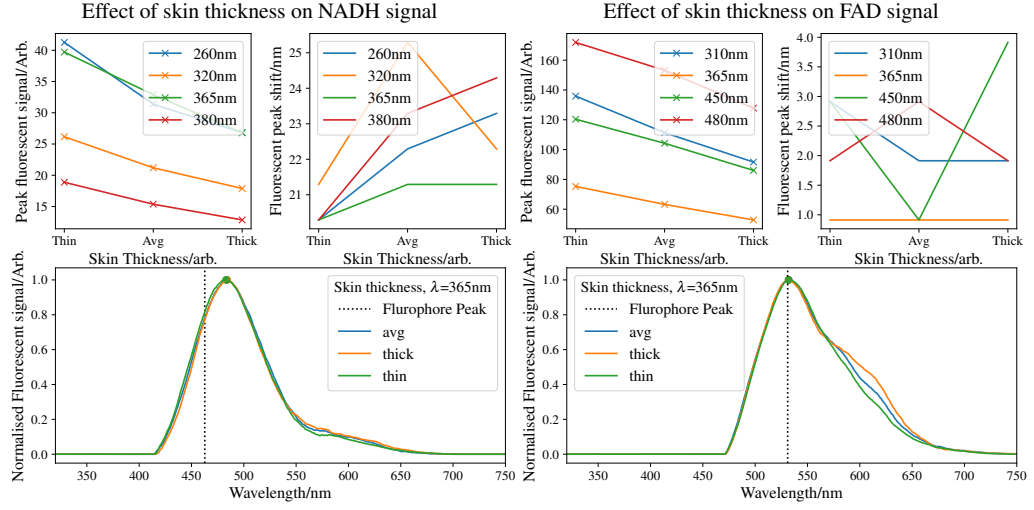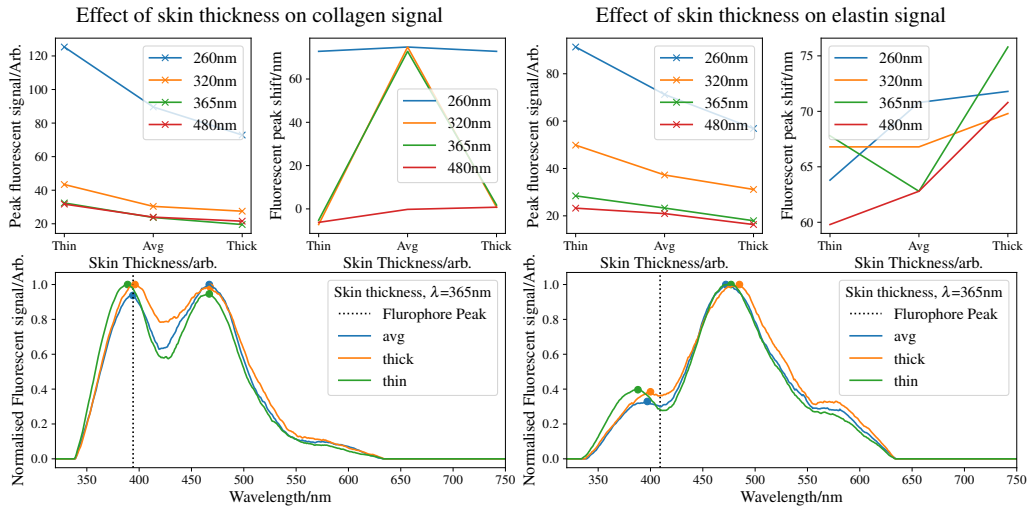***Figure 1.30:*** *Effect of thickness on elastin (left) and collagen (right) autofluorescence. Top left of each image shows the effect of skin thickness on signal strength. Top right of each image shows the effect of skin thickness on location of the fluorophores peak. Bottom of each image shows the raw spectra for 365 nm.*

1.6.3   Using the NM Method

We model the experimental setup by S. Smirni *et al.* as described in a previous section. The computational speed ups described in the validation sections are also used. The 5 layers skin model is setup with NADH, FAD and collagen distributed in different layers. NADH and FAD are initially in all layers except the hypodermis, and collagen is contained in just the papillary and reticular dermis[**]. Each layer has its own concentration of the fluorophores giving n for the NM method of 10. An initial guess of the concentration of the fluorophores is made, and the NM method is allowed to run until it stagnates. The target spectrum for the NM is taken from S. Smirni experimental data. Before the target spectrum could be used it was first "cleaned up". This "cleaning" process was required as the spectrum was shifted by 20 nm into larger wavelengths. The cause of this systematic shift is unknown. As a backscatter peak is included within the spectrum, the spectrum can be moved to its correct position. The next step in the "cleaning" process is to filter out spectra that are "defective". Several of the autofluorescence spectra have artificial peaks caused by various experimental errors or machine faults. The final stage of the "cleaning" process, is to smooth the data out and remove the backscatter peak. Now the spectra can be used as a target spectrum for the NM method.

Figure 1.31 shows the output of the NM method during a run with the above parameters. The figure shows that as the simplex iterates, the average fitness improves, the average number of calls to the MCRT algorithm tends to ~ 1.4. This suggests that the NM keeps the reflected point more often than not. The size of the simplex fluctuates as the simplex tries to find the global minima. This happens as the simplex moves over the search space it sometimes needs to grow in size, then when it finds a minimum it shrinks around it. The size of the simplex will then grow when the algorithm is restarted.
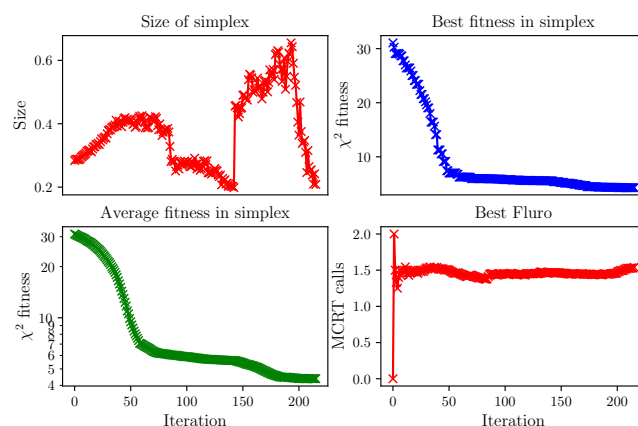
Figure 1.31: *Figure shows the diagnostic information output by the NM method. Top left) shows the size of the simplex as it evolves. Top right) shows the best point in the simplex as it evolves. Bottom left) shows the average fitness of the simplex. Bottom right) shows the number of calls to the MCRT code per iteration of the simplex. The more call to the MCRT the simplex requires, the longer the runtime.*

Figure 1.32 shows the output of the NM. The "best" fitness achieved by the algorithm was ~ 3, which is a fairly poor fit when compared to the validation examples above. The figure also shows the contribution of the individual fluorophores to the overall autofluorescence signal.

[**]We omit any fluorophores form the hypodermis as they are not expected to contribute to the signal at all, or by much. This also simplifies the problem from n=13 to n=10.

As expected the main contribution is from NADH, with a little contribution by FAD. However, collagen contributes to the main peak and is multi-peaked, with peaks at ∼380 nm and ∼ 465 nm. This is unusual as the peak of emission for collagen used in this work is around 395 nm, therefore it was not expected to contribute to the signal around the NADH peak. The reason that the collagen signal is multi-peaked is due to the tissue optics. There is a large peak at around 400–410 nm in the absorption spectra in the dermal layers. This causes a dip in the emission of collagen, giving it the multi-peaked profile.
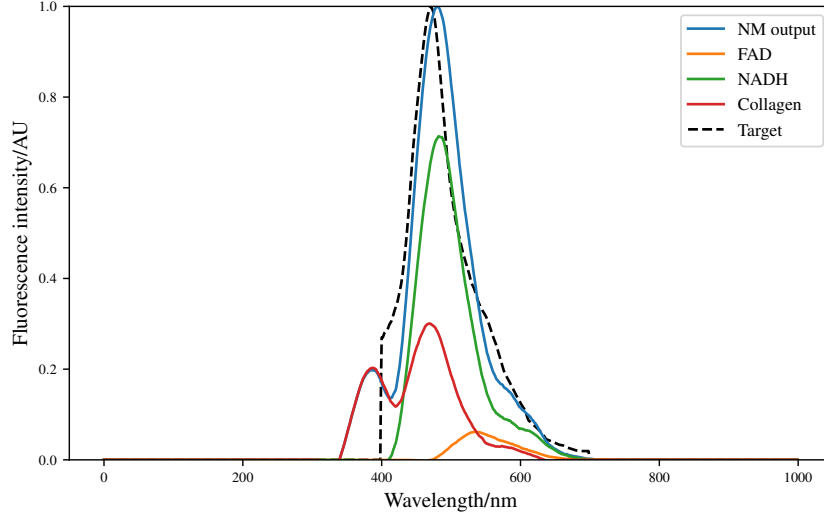
Figure 1.32: *Figure shows the best result from the NM operating on the experimental data from S. Smirni et al.. The spectrum has a fitness of ∼ 3. The figure also shows the makeup of the final spectrum by the individual fluorophores.*

1.7 Discussion

There are several probable reasons why the spectrum generated by the MCRT and NM does not match the experimental data exactly. A first possible reason for the mismatch, is that the optical properties of the fluorophores are not accurately known. Optical properties of the fluorophores used in the work are not readily available. There are various sources that have measured them, but they are usually confined to several wavelengths of the authors interest and not a full spectrum. The extinction coefficients for the fluorophores are measured in various buffer solutions, and not taken from *in-vivo* tissue. This could give rise to a discrepancy between the computed results and the experimental results. The emission spectra for the fluorophores could also be incorrect. Emission spectra used in this work are also measured in various buffer solutions, which again may be different from what they are *in-vivo*. Finally the emission spectra are measured for a single excitation wavelength. As the spectra were not readily available for the excitation wavelength used in this work, the emission spectra were taken from the nearest possible excitation wavelength found in the literature. This again may introduce a difference from the experimental work. However, what optical properties that have been published are pretty consistent from author to author therefore, this is an unlikely problem.

The mismatch in the target spectrum and the calculated spectrum could be due to missing fluorophores. The model presented here only included NADH, FAD, and collagen which are

thought to be the three main contributors to the autofluorescence signal. However, the inclusion of riboflavin (peak at 529 nm), β-carotene (395 nm), elastin (425 nm), and different types of collagen (420, 370, 395 nm) may be able to correct this.

A final possible reason for the mismatch is that the LAKK-M device creators seem to have mis-calibrated their machines for finding the peaks of various fluorophores. Table 1.5 shows a comparison between the literature and the values used by the LAKK-M team.

Fluorophore	LAKK-M peak/nm	Literature peak/nm
FAD	550	525
NADH	490	465
Elastin	450	425
Collagen	420	370(IV), 395(I,V), 600(VII)

Table 1.5: *Comparison of LAKK-M emission peaks and that found in the literature. AS there are different types of collagen multiple types were included in the literature comparison. LAKK-M data from [48–51]. Literature values taken from [38, 41, 52, 53].*

For whatever reason, they seem to be consistently off by around 25 to 30 nm. From this chapter's work on how tissue optics affects the fluorescent signal, tissue optics cannot account for the discrepancy. One possible cause for this is that the UV light they use to probe autofluorescence is an LED. LED light sources are not monochromatic, but rather have a range of wavelengths they emit, on the order of 25 nm FWHM. Therefore, they could be exciting with a different range of wavelengths, which could possibly contribute towards the difference in what they measure and the literature values.

1.8   Conclusion

In conclusion, this section has introduced a five layer skin model, that has the ability to vary the various constituent parts to tailor a model for a generic or specific patient. We have also shown in this chapter a method of coupling an optimisation technique to MCRT. This was done in order to investigate the concentrations of naturally occurring fluorophores in the skin. Differing levels of the fluorophores can indicate various diseases such as diabetes and CVDs. We validated this technique against a toy model in various dimensions, with good agreement. Before experimental data was analysed, the effect of tissue optics on the autofluorescent signal was tested. We found that both blood and melanin can have a large effect on the autofluorescent signal. We found that melanin acts as a block to light penetrating into the skin and can shift the detected signal into the red end of the spectrum. The simulations showed that blood changes the detected spectrum drastically, by introducing multiple peaks into the autofluorescent signal for several fluorophores, along with shifting detected peaks of several fluorophores. We then used our numerical model on experimental data. We found good, but not excellent agreement with the data. A discussion of why our model does not fit the experimental data, with several possible reasons presented. Future work would involve taking known "good" data that would be worthwhile to validate against. Finally, if the model can be validated against this data the model could be used in future to explore the relationship between various diseases and autofluorescence.

Chapter 2

Conclusion

2.1 Summary

To summarise this thesis, the MCRT method is a powerful technique that can be used to calculate the transport of light (as particles or quasi-wave/particles) through turbid media, whilst modelling multiple anisotropic scattering alongside a variety of microphysics. The only downsides to the MCRT method noted in the literature (as well as discussed at length in this thesis) is the computational load required for some problems, and the selection of optical properties. With the growing power of computational devices, the computational load of MCRT becomes less of a factor. Likewise the optical properties of various biological tissues, are now increasingly being measured with greater precision and accuracy.

Chapter 1 introduced the concept at the heart of this thesis, the Monte Carlo method. The chapter gave examples of how the Monte Carlo method can be used to sample from spectra, and how it is can be used to model various physical events. Chapter 2 followed on from chapter 1's explanation of the Monte Carlo method, by introducing MCRT used in all subsequent chapters. Chapter 2 also covered the theory behind the method and presented details of the implementation of the method into code as well as various computational speedups utilised.

Chapter 3 described the application of the MCRT method to modelling tissue ablation. Details of how the MCRT was coupled to a numerical model of heat diffusion and thermal damage model was presented. The chapter showed that we can successfully model experimental and theoretical data with our numerical model. The power the model has is that we can predict thermal damage, and ablation crater size for any laser, and configuration thereof, without the need to test on humans or animals. It also allows the testing of different lasers without the purchase of said laser, which could allow clinicians to "try before they buy". The chapter also presented (with tongue firmly in cheek) the application of this numerical model to humane spy disposal.

Chapter 4 presented the modification of the MCRT method, such that it would allow the modelling of the photon packets as quasi-wave/particle packets, in place of the usual particle model the MCRT method models. This was achieved via a few small changes within the code, based upon well understood theoretical models namely the Fresnel-Huygens principle. The method was thoroughly validated against several theoretical expressions. The method was also validated against experimental results from collaborators at the University of Dundee. The new method was then used to compare Bessel and Gaussian beams performance in highly turbid media, to see which beam preformed "better".

Chapter 5 presented a model of skin autofluorescence using MCRT. The chapter detailed a five layer skin model created to approximate the skin. The five layer model included the various chromophores found in the skin such as blood, water, and melanin. The model also includes various naturally occurring fluorophores. Changes in the autofluorescent response of tissue has been shown to be indicative of various diseases. However, details of how each fluorophore contributes to the signal is not well understood. Therefore, a study on how tissue optics affects the autofluorescent signal, and how much each fluorophore contributes was undertaken. The MCRT algorithm was also coupled to an optimisation technique to determine relative concentrations of the fluorophores in the skin from a given autofluorescent signal. The technique chosen was the Nelder-Mead method. The NM method uses simplices in order to move around the search space and find global minima. The method was coupled to the MCRT algorithm and validated against toy models. Finally details of how autofluorescent data from collaborators was analysed using these techniques was presented.

2.2   Future Prospects

There are several avenues of promising work that can continue on from this thesis.

The code developed as part of the tissue ablation chapter, could easily be adapted for use in modelling photothermal therapy. Photothermal therapy is the use of light to selectively heat up nanoscale materials that have been inserted into tumours. The nanoscale materials, such as gold nanorods, are targeted with a specific wavelength of light (usually near infra-red) which heats up the rods and thus the surrounding tissue, eventually killing the adjacent cells [54, 55]. This could be easily modelled within the code developed as part of chapter 3, with little to no major changes. The code could be used to help optimise photothermal treatment modalities and predict treatment outcomes.

There is also scope to improve the heat transfer model. As mentioned in the chapter, a simple explicit model was used as it is relatively easy to setup and solve a given problem using this scheme. However, this scheme leads to constraints on the timestep. This could be avoided by using an implicit scheme which is unconditionally stable for any timestep. Another way the heat transfer model could be improved is through the use of the finite element method (FEM). The FEM allows PDEs to be solved on arbitrary grids, which would reduce the high memory requirement our model needs to achieve good resolution. The FEM would also allow a more accurate skin model to be included within the simulation, making the simulation more realistic.

Finally, the work of chapter 3 could also be extended to include a drug diffusion model. One use of tissue ablation is as an optical drill to create micro holes in the skin. These holes in the skin then allow better penetration of topical drugs. Modelling both the laser tissue ablation process and drug diffusion process in one simulation would allow *in-silico* testing of treatment parameters which could easily be optimised by the model.

The algorithm developed as part of chapter 4's work, φMC, also has several avenues of future research. It should be fairly easy to extend the algorithm to model other beams, such as an Airy beam. It should also be fairly trivial to implement a spatial light modulator (SLM). An SLM is a device that can modulate light that is incident on it including imparting phase to different parts of the incident beam. This allows arbitrary complex beams to be created. The ability to model an SLM would open up the ability to model complex experiments in such things as wavefront shaping. Other types of experiments the algorithm could be used for include: laser speckle imaging, focusing light though turbid media, and complex micromanipulation [56–58].

One obvious avenue of future research would be to improve the five layer skin model presented as part of chapter 5's work. The skin model presented is planar, where as tissue is not planar

34

in any sense. The first improvement on this could be to introduce a more complex geometrical structure into the voxel model. However, this method would quickly run into a computational wall. To represent the non planar reality of the tissue would require many voxels, such that the RAM required to run any simulation would be prohibitive to running the simulations. Therefore, a different geometrical model would need to be used. A solution to this was briefly investigated: use of a mesh to model the skin's structure. Triangular meshes can be used to approximately model any arbitrary shape or volume. The use of triangular meshes have been used to great effect by other authors in MCRT codes. Due to time constraints this was abandoned for this thesis before a fully working code could be developed. Figure 2.1 shows MCRT being preformed on a gourd made from a triangular mesh using the code developed as part of testing this method.
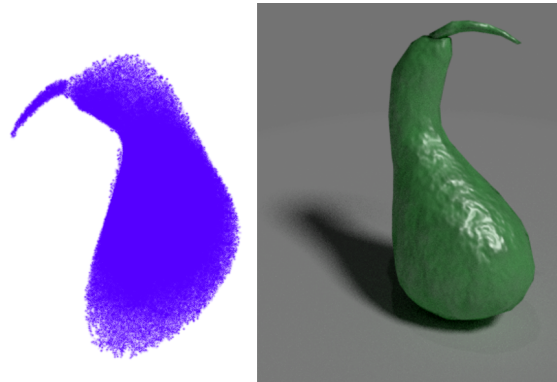

Figure 2.1: *Image on the left shows the fluence of light in a gourd, calculated using MCRT. The optical properties of the gourd in this simulations are similar to that of skin. The optical properties of the medium around the gourd are that of air. Image on the right shows a rendering of the same mesh in blender.*

A meshed skin model would allow objects like hairs, blood vessels, sweat glands, and the uneven boundaries between skin layers greatly increasing the accuracy of the simulations.

Finally as the data from our collaborators equipment was not of a quality such that it could be reproduced using amoebaMCRT, this data could be taken again with better equipment, or other authors could be found that have the requisite data. AmoebaMCRT would then be run on this data to determine the amount that each fluorophore contributes to the signal. Other optimisation techniques other than the NM method could also be explored. Techniques such as simulated annealing, genetic algorithms* or machine learning could be used. It could also be possible for our MCRT code to be used to create a "bank" of spectra that could then be used to train a machine learning algorithm to label peaks, and contributions to those peaks by fluorophores.

---

*The use of genetic algorithms was explored, however the computational cost of using them was deemed too high.

Bibliography

[1] World Health Organisation. *Cardiovascular diseases (CVDs)*, 17 May 2017 (accessed June 16, 2019). https://www.who.int/en/news-room/fact-sheets/detail/cardiovascular-diseases-(cvds).

[2] P. Bhatnagar, K. Wickramasinghe, E. Wilkins, and N. Townsend. Trends in the epidemiology of cardiovascular disease in the uk. *Heart*, 102(24):1945–1952, 2016.

[3] R.S. Vasan. Biomarkers of cardiovascular disease: molecular basis and practical considerations. *Circulation*, 113(19):2335–2362, 2006.

[4] M.H. Olsen. Assessment of cardiovascular risk â the impact and future of non-traditional cardiovascular risk markers. 2010.

[5] A.R. Folsom. Classical and novel biomarkers for cardiovascular risk prediction in the united states. *Journal of epidemiology*, page JE20120157, 2013.

[6] N. Kollias, R. Gillies, M. Moran, I.E Kochevar, and R.R Anderson. Endogenous skin fluorescence includes bands that may serve as quantitative markers of aging and photoaging. *Journal of investigative dermatology*, 111(5):776–780, 1998.

[7] M. Monici. Cell and tissue autofluorescence research and diagnostic applications. *Biotechnology annual review*, 11:227–256, 2005.

[8] E. Drakaki, E. Kaselouris, M. Makropoulou, A.A Serafetinides, A. Tsenga, A.J Stratigos, A.D Katsambas, and C. Antoniou. Laser-induced fluorescence and reflectance spectroscopy for the discrimination of basal cell carcinoma from the surrounding normal skin tissue. *Skin pharmacology and physiology*, 22(3):158, 2009.

[9] Y. Pu, W. Wang, Y. Yang, and R.R. Alfano. Native fluorescence spectra of human cancerous and normal breast tissues analyzed with non-negative constraint methods. *Applied optics*, 52(6):1293–1301, 2013.

[10] N. Ramanujam. Fluorescence spectroscopy of neoplastic and non-neoplastic tissues. *Neoplasia*, 2(1-2):89–117, 2000.

[11] M. Tarnawska, K. Dorniak, M. Kaszubowski, M. Dudziak, and M. Hellmann. A pilot study with flow mediated skin fluorescence: A novel device to assess microvascular endothelial function in coronary artery disease. *Cardiology journal*, 25(1):120–127, 2018.

[12] R.P. van Waateringe, B.T. Fokkens, S.N. Slagter, M.M. van der Klauw, J.V. van Vliet-Ostaptchouk, R. Graaff, A.D. Paterson, A.J. Smit, H.L. Lutgers, and B.H.R. Wolffenbuttel. Skin autofluorescence predicts incident type 2 diabetes, cardiovascular disease and mortality in the general population. *Diabetologia*, 62(2):269–280, 2019.

[13] N. Akbar, S. Sokolovski, A. Dunaev, J.J.F. Belch, E. Rafailov, and F. Khan. In vivo noninvasive measurement of skin autofluorescence biomarkers relate to cardiovascular disease in mice. *Journal of microscopy*, 255(1):42–48, 2014.

[14] M.M. Elahi, Y.X. Kong, and B.M. Matata. Oxidative stress as a mediator of cardiovascular disease. *Oxidative medicine and cellular longevity*, 2(5):259–269, 2009.

[15] T.S. Blacker and M.R. Duchen. Investigating mitochondrial redox state using nadh and nadph autofluorescence. *Free Radical Biology and Medicine*, 100:53–65, 2016.

[16] A.C. Croce and G. Bottiroli. Autofluorescence spectroscopy and imaging: a tool for biomedical research and diagnosis. *European journal of histochemistry: EJH*, 58(4), 2014.

[17] I.M. Freedberg and T.B. Fitzpatrick. *Fitzpatrick's Dermatology in General Medicine*. Number v. 2 in Fitzpatrick's Dermatology in General Medicine. McGraw-Hill, Health Professions Division, 1999.

[18] Z. Zaidi and S.W. Lanigan. *Dermatology in Clinical Practice*. Springer London, 2010.

[19] S. Prahl. *Tabulated Molar Extinction Coefficient for Hemoglobin in Water*, 1999 (accessed June 15, 2019). https://omlc.org/spectra/hemoglobin/summary.html.

[20] D.M. Wieliczka, S. Weng, and M.R. Querry. Wedge shaped cell for highly absorbent liquids: infrared optical constants of water. *Applied optics*, 28(9):1714–1719, 1989.

[21] D.J. Segelstein. *The complex refractive index of water*. PhD thesis, University of Missouri–Kansas City, 1981.

[22] S.L. Jacques, I.S. Saidi, A. Ladner, and D. Oelberg. Developing an optical fiber reflectance spectrometer to monitor bilirubinemia in neonates. In *Laser-Tissue Interaction VIII*, volume 2975, pages 115–125. International Society for Optics and Photonics, 1997.

[23] S. Prahl. *Tabulated Molar Extinction Coefficient for Bilirubin in chloroform*, 2017 (accessed June 15, 2019). https://omlc.org/spectra/PhotochemCAD/html/119.html.

[24] S. Prahl. *Tabulated Molar Extinction Coefficient for Beta-carotene in hexane*, 2017 (accessed June 15, 2019). https://omlc.org/spectra/PhotochemCAD/html/041.html.

[25] J.A Iglesias-Guitian, C. Aliaga, A. Jarabo, and D. Gutierrez. A biophysically-based model of the optical properties of skin aging. In *Computer Graphics Forum*, volume 34, pages 45–55. Wiley Online Library, 2015.

[26] I.S Saidi et al. *Transcutaneous optical measurement of hyperbilirubinemia in neonates*. PhD thesis, Rice University, 1992.

[27] I.V. Meglinski and S.J. Matcher. Quantitative assessment of skin layers absorption and skin reflectance spectra simulation in the visible and near-infrared spectral regions. *Physiological Measurement*, 23(4):741, 2002.

[28] S.L Jacques. Optical properties of biological tissues: a review. *Physics in Medicine & Biology*, 58(11):R37, 2013.

[29] A. Krishnaswamy and G.V.G Baranoski. A biophysically-based spectral model of light interaction with human skin. In *Computer Graphics Forum*, volume 23, pages 331–340. Wiley Online Library, 2004.

[30] C.L Campbell, C. Christison, C.T.A Brown, K. Wood, R.M. Valentine, and H. Moseley. 3d monte carlo radiation transfer modelling of photodynamic therapy. In *Biophotonics South America*, volume 9531, page 95311H. International Society for Optics and Photonics, 2015.

[31] C. Campbell. *Under the skin: Monte Carlo radiation transfer modelling of photodynamic therapy*. PhD thesis, School of Physics and Astronomy, University of St Andrews, 2016.

[32] M.J.C Van Gemert, S.L Jacques, H.J.C.M Sterenborg, and W.M. Star. Skin optics. *IEEE Transactions on biomedical engineering*, 36(12):1146–1154, 1989.

[33] R. Gillies, G. Zonios, R.R Anderson, and N. Kollias. Fluorescence excitation spectroscopy provides information about human skin in vivo. *Journal of Investigative Dermatology*, 115(4):704–707, 2000.

[34] S. Prahl. *Tabulated Molar Extinction Coefficient for Tyrosine in water, 0.1 M phosphate buffer, pH 7*, 2017 (accessed June 16, 2019). https://omlc.org/spectra/PhotochemCAD/html/092.html.

[35] S. Prahl. *Tabulated Molar Extinction Coefficient for Tryptophan in water, 0.1 M phosphate buffer, pH 7*, 2017 (accessed June 16, 2019). https://omlc.org/spectra/PhotochemCAD/html/091.html.

[36] S. Soltani, A. Ojaghi, and F.E Robles. Deep uv dispersion and absorption spectroscopy of biomolecules. *Biomedical optics express*, 10(2):487–499, 2019.

[37] Y. Sun, Y. Pu, Y. Yang, and R.R. Alfano. Biomarkers spectral subspace for cancer detection. *Journal of biomedical optics*, 17(10):107005, 2012.

[38] M. Islam, M. Honma, T. Nakabayashi, M. Kinjo, and N. Ohta. ph dependence of the fluorescence lifetime of fad in solution and in cells. *International journal of molecular sciences*, 14(1):1952–1963, 2013.

[39] E.W Evans, C.A Dodson, K. Maeda, T. Biskup, C.J. Wedge, and C.R. Timmel. Magnetic field effects in flavoproteins and related systems. *Interface focus*, 3(5):20130037, 2013.

[40] A. Von Ketteler, D.P Herten, and W. Petrich. Fluorescence properties of carba nicotinamide adenine dinucleotide for glucose sensing. *ChemPhysChem*, 13(5):1302–1306, 2012.

[41] R.S DaCosta, H. Andersson, and B.C Wilson. Molecular fluorescence excitation–emission matrices relevant to tissue spectroscopy. *Photochemistry and photobiology*, 78(4):384–392, 2003.

[42] F. Gao and L. Han. Implementing the nelder-mead simplex algorithm with adaptive parameters. *Computational Optimization and Applications*, 51(1):259–277, 2012.

[43] W.H. Press and S.A. Teukolsky. Savitzky-golay smoothing filters. *Computers in Physics*, 4(6):669–672, 1990.

[44] T.B Fitzpatrick. The validity and practicality of sun-reactive skin types i through vi. *Archives of dermatology*, 124(6):869–871, 1988.

[45] Y. Lee and K. Hwang. Skin thickness of korean adults. *Surgical and radiologic anatomy*, 24(3-4):183–189, 2002.

[46] P. Oltulu, B. Ince, N. Kökbudak, F. Kılıç, et al. Measurement of epidermis, dermis, and total skin thicknesses from six different body regions with a new ethical histometric technique. *Türk Plastik, Rekonstrüktif ve Estetik Cerrahi Dergisi (Turk J Plast Surg)*, 26(2):56–61, 2018.

[47] W.F.W Southwood. The thickness of the skin. *Plastic and Reconstructive Surgery*, 15(5):423–429, 1955.

[48] S. Palmer, K. Litvinova, A. Dunaev, S. Fleming, D. McGloin, and G. Nabi. Changes in autofluorescence based organoid model of muscle invasive urinary bladder cancer. *Biomedical optics express*, 7(4):1193–1200, 2016.

[49] A.V Dunaev, V.V Dremin, E.A Zherebtsov, I.E Rafailov, K.S Litvinova, S.G Palmer, N.A Stewart, S.G Sokolovski, and E.U Rafailov. Individual variability analysis of fluorescence parameters measured in skin with different levels of nutritive blood flow. *Medical engineering & physics*, 37(6):574–583, 2015.

[50] O.D Smirnova, D.A Rogatkin, and K.S Litvinova. Collagen as in vivo quantitative fluorescent biomarkers of abnormal tissue changes. *Journal of Innovative Optical Health Sciences*, 5(02):1250010, 2012.

[51] S.G Palmer. *Development of Non-invasive Techniques for Bladder Cancer Diagnosis and Therapy*. PhD thesis, University of Dundee, 2016.

[52] YL. Pan. Detection and characterization of biological and other organic-carbon aerosol particles in atmosphere using fluorescence. *Journal of Quantitative Spectroscopy and Radiative Transfer*, 150:12–35, 2015.

[53] G.H Patterson, S.M Knobel, P. Arkhammar, O. Thastrup, and D.W Piston. Separation of the glucose-stimulated cytoplasmic and mitochondrial nad (p) h responses in pancreatic islet β cells. *Proceedings of the National Academy of Sciences*, 97(10):5203–5207, 2000.

[54] M. Singh, D.C.C Harris-Birtill, Y. Zhou, M.E Gallina, A.E.G Cass, G.B Hanna, and D.S Elson. Application of gold nanorods for photothermal therapy in ex vivo human oesophagogastric adenocarcinoma. *Journal of biomedical nanotechnology*, 12(3):481–490, 2016.

[55] M.E Gallina, Y. Zhou, C.J Johnson, D. Harris-Birtill, M. Singh, H. Zhao, D. Ma, T. Cass, and D.S Elson. Aptamer-conjugated, fluorescent gold nanorods as potential cancer theradiagnostic agents. *Materials Science and Engineering: C*, 59:324–332, 2016.

[56] I.M Vellekoop and A.P Mosk. Focusing coherent light through opaque strongly scattering media. *Optics letters*, 32(16):2309–2311, 2007.

[57] R. Horstmeyer, H. Ruan, and C. Yang. Guidestar-assisted wavefront-shaping methods for focusing light into biological tissue. *Nature photonics*, 9(9):563, 2015.

[58] T. Čižmár, M. Mazilu, and K. Dholakia. In situ wavefront correction and its application to micromanipulation. *Nature Photonics*, 4(6):388, 2010.